DOI: 10.24850/j-tyca-2025-02-02

Articles

Numerical modeling of skimming flow in a stepped channel with vertical curves

Modelación numérica del flujo rasante en un canal escalonado con curvas verticales

Daniel López-de-Mesa[1], ORCID: https://orcid.org/0000-0002-7577-5527

Andrés Felipe Cuervo[2], ORCID: https://orcid.org/0009-0004-9192-6964

Alejandra Balaguera[3], ORCID: https://orcid.org/0000-0002-4552-513X

[1]Universidad de Medellín, Faculty of Engineering, Antioquia, Colombia, dlopez@udemedellin.edu.co

[2]Universidad de Medellín, Faculty of Engineering, Antioquia, Colombia, afcuervov@gmail.com

[3]Universidad de Medellín, Faculty of Engineering, Antioquia, Colombia, abalaguera@udemedellin.edu.co

Corresponding author: Daniel López-de-Mesa, dlopez@udemedellin.edu.co

Abstract

Stepped channels are frequently used for the discharge of water in reservoirs, however, there are few studies that consider the implementation of curves at their bottom. This article presents a quantitative evaluation, using numerical modeling with computational fluid dynamics (CFD), of the properties of skimming flow in steep stepped chutes with vertical curves. The stepped geometry was defined with a convex curve at the inlet, an intermediate straight chute, and a concave curve at the outlet. A comparative analysis was performed on the velocity, pressure, vorticity, and turbulence statistics fields in the three sections of the channel. It was concluded that the velocity profiles obtained with the RNG k-ε turbulence model presented a good agreement with experimental measurements in the non-aerated flow zone. However, the correlation decreased downstream since the numerical model did not capture the aeration phenomenon. When comparing the hydrodynamic behavior in both stepped curves, it was found that the separation zone covered a greater fraction of each step in the convex curve. In the latter, negative pressure values were observed at the height of the upper corner of the risers, which were not present in the concave curve. Finally, the turbulent dissipation maxima were found near the bottom in the final section of the treads, and on the border between the main stream and the recirculating flow of each step, being higher for the outlet curve.

Keywords: Skimming flow, stepped channel, stepped spillway, vertical curves, computational fluid dynamics (CFD), turbulence, turbulent dissipation.

Resumen

Los canales escalonados se utilizan frecuentemente para la descarga de agua en embalses, sin embargo, hay pocos estudios que consideren la implementación de curvas en el fondo de este tipo de estructuras. Este artículo presenta una evaluación cuantitativa, mediante modelación numérica con dinámica de fluidos computacional (CFD), de las propiedades del flujo rasante en canales escalonados de alta pendiente con curvas verticales. La geometría escalonada se definió con una curva convexa a la entrada, una rampa recta intermedia y una curva cóncava a la salida, con el fin de comparar los campos de velocidad, presión, vorticidad y estadísticas de la turbulencia en los tres tramos del canal. Se concluyó que los perfiles de velocidad obtenidos con el modelo de turbulencia RNG k-ε presentaron una buena correlación con mediciones experimentales en la zona de flujo no aireada. Sin embargo, la calidad del ajuste disminuyó aguas abajo, ya que el modelo numérico no capturó el fenómeno de aireación. Al comparar el comportamiento hidrodinámico en ambas curvas escalonadas se encontró que la zona de separación abarcó una mayor fracción de cada escalón en la curva convexa. En ésta se presentaron además valores negativos de presión a la altura de la esquina superior de las contrahuellas, los cuales no se evidenciaron en la curva cóncava. Finalmente, los máximos de disipación turbulenta se encontraron cerca del fondo en el tramo final de las huellas, y en la frontera entre la corriente principal y el flujo recirculante de cada escalón, y fueron mayores para la curva a la salida del canal.

Palabras clave: flujo rasante, canal escalonado, vertedero escalonado, curvas verticales, dinámica de fluidos computacional (CFD), turbulencia, disipación turbulenta.

Received: 04/07/2023

Accepted: 10/30/2023

Introduction

A stepped chute is an open channel with a series of falls or steps at the bottom. The slope of the channel is determined by the ratio of the height of the riser to the length of the tread of each step. There are three flow regimes: nappe, transition, and skimming. Nappe flow is characterized by successive free-falling jets, with an air gap between the jet and the riser. In skimming flow, the main stream passes over the pseudo-bottom, which is defined as the imaginary line joining the outer corners of the steps, which act as a macro roughness (Chanson, 1994). Finally, transition flow is an intermediate condition between the two previous ones, in which the air chamber appears in some steps and not in others, and the free surface has a chaotic behavior with certain regions of water splashing (Chanson & Toombes, 2004).

The use of stepped spillways intensified thanks to the progress shown by the industry in the handling of roller-compacted concrete since the end of the 20th century (Chanson, 2001). The latter, added to the fact that skimming flow occurs with large discharges or high slopes (Chanson, 1994), frequently occurring in the spillways of large reservoirs, has generated in recent years a growing interest of researchers in describing qualitatively and quantitatively the hydrodynamics of this flow regime. At a qualitative level, Chanson (1994) found that under the pseudo-bottom, recirculation vortices form in the cavities between the tread and the riser, which are maintained by the transfer of stresses from the main stream. If the tread is long enough, downstream of the vortices, the main flow reattaches to the surface of the steps. The same author and Llano (2003) reported that initially, starting from the first step, the non-aerated region of the flow is present, with a free surface of smooth appearance. At the bottom, the steps generate turbulence, and the boundary layer grows until it intercepts the free surface at the so-called air inception point (AIP). Downstream, turbulence levels are high enough to generate the aerated flow region.

The quantitative description of both aerated and non-aerated regions has been based mainly on the analysis of velocity, pressure, and energy dissipation fields. Bombardelli, Meireles and Matos (2011) recorded flow velocity and depth measurements in a physical model of a high-slope stepped spillway upstream of the AIP and compared with numerical CFD results using the $k - \varepsilon$ and RNG $k - \varepsilon$ turbulence models. Their boundary layer growth rate results proved to be higher than those reported by other research on smooth discharges. Likewise, their analysis of turbulence statistics showed the maximum values of turbulent kinetic energy and turbulent dissipation in the center of stepped cavities, increasing in the flow direction due to boundary layer development. In a similar study, Nikseresht, Talebbeydokhti and Rezaei (2013) used $k-\varepsilon$, $k-\omega$ and Reynolds Stress type turbulence models to analyze the skimming flow field in a stepped spillway of 1H:1V slope, validating the results with the measurements of Chinnarasri and Wongwises (2006). The authors reported recirculation vortices occupying the entire stepped cavities, with negative pressure values near the top corner of the risers. They considered these points to be critical positions because they are more prone to cavitation phenomena. Medhi, Singh, Thokchom and Mahapatra (2019) studied the velocity distributions in the aerated and non-aerated flow regions, also for a 1H:1V slope, using experimental image processing techniques, and CFD numerical modeling with the $k-\varepsilon$ model. The authors' results showed at higher flow rates, the displacement of the AIP downstream, implying a longer length of the non-aerated region. In general, the maximum velocities in the flow field coincided approximately with an intermediate depth, close to the pseudo-bottom.

The above are only some of the investigations reported in the literature, presented for having stepped structures with similar slope to the one to be analyzed in this study, or for using equivalent methodologies, so they will serve as a point of comparison for the results obtained here. Skimming flow is in general a mature subject in the state of the art, which has been extensively studied since the previous century, then, in the last decade research efforts have focused on geometric variations of the stepped bottom. This is the case of Zare and Doering (2012), who analyzed the effect of rounded edges at the step tips, or Arjenaki and Sanayei (2020), who compared the flow over typical steps with a horizontal tread, with cases of inclined tread in the spanwise direction. In the present article, for example, the progressive variation of the tread length will be applied to conform stepped vertical curves at the entrance and the exit of the channel.

Regarding this subject of study, it is typical in the design of smooth spillways to use a convex curve at the inlet that adjusts to the flow path as it leaves the upper crest, and a concave curve at the outlet to minimize the pressures exerted on the bottom of the channel (Bureau of Reclamation, 1987). However, in the literature review there are few studies that address the hydrodynamics of flow in a stepped configuration that conforms to this type of curve. First, Tabbara, Chatila and Awwad (2005) analyzed the skimming flow in a high-slope stepped weir with convex and concave curves at the inlet and outlet, respectively, by numerical modeling based on the $k-\varepsilon$ turbulence model. In both, curved-shaped flow depth profiles, like that of the pseudo-bottom, and recirculation vortices fully occupying the steps were reported, regardless of the ratio between tread and riser sizes. In addition, the maximum pressure values were reported in the final fraction of the treads. It should be clarified that the authors did not highlight significant flow differences in both curves. In the studies of Attari and Sarfaraz (2012); Sarkardeh, Marosi and Roshan (2015); Henrique Povh and Junji Ota (2019); and Dalili Khanghah and Kavianpour (2020), only the convex curve at the inlet and the importance of including in it transition steps (with incremental magnitudes downstream) were considered, to prevent the occurrence of flow jumps in the transition from the curve to the straight section of the spillway. In addition, when comparing a stepped curve with a smooth curve, lower flow velocities were found for the former in the initial section of the spillway, and a lower risk of cavitation upstream of the AIP.

Finally, the investigations of Ashoor and Riazi (2019), and Zuhaira, Al-Hamd, Alzabeebee and Cunningham (2021) are the most similar to our work, since they comparatively analyzed the skimming flow in stepped weirs with concave and convex shape. However, they considered the entire structure with one of the two shapes, while in the present study both vertical curves were distributed at the inlet and outlet of the same channel. In contrast to Tabbara *et al.* (2005), the authors reported relevant differences between both bottom configurations, e.g., the free surface of the flow was again described with a shape like the curved geometry of the spillway, but they found an air gap only in the first step of the concave case. This demonstrated the importance of a convex curve at the inlet to prevent flow detachment. Additionally, to match the steps with the curves, longer treads were required at the end of the concave bottom and shorter treads at the convex one. This detail implied vortices of greater magnitude in the former, which led to greater energy dissipation and, consequently, lower velocity at the exit of the structure. Thus, the decisive role of the fraction of each step that is occupied by the recirculating flow, and therefore also of the remaining fraction occupied by the reattached flow, in the magnitude of the hydrodynamic variables in the steps, became evident.

Considering the previously reported literature results and the knowledge gaps and given a steady flow regime in a steeply sloping stepped channel with three sections: a convex curve at the inlet, an intermediate straight chute, and a concave curve at the outlet, this paper analyzed for the first time the differences in flow hydrodynamics in these three regions, distributed along the same stepped structure. For this purpose, the objectives of the present study were defined as follows: 1) analyze the fraction of the steps occupied by the vortex region vs. the reattached flow region, 2) define the difference in the distribution of velocity, pressure, vorticity and turbulence statistics in these regions, and 3) compare the hydrodynamics of the flow in the three sections of the channel based on the variables of objectives 1 and 2.

Materials and methods

Experimental data

The experimental data for validation of the numerical model were obtained from measurements reported by Hunt and Kadavy (2010a), and Hunt and Kadavy (2010b). Figure 1 shows the experimental setup, which consists of a channel with a width of 1.83 m, a wide crest of 2.40 m in length, and a stepped section of 6.10 m in length measured in the x direction. The total vertical fall is 1.5 m, with steps composed of treads of length l of 152 mm, and risers of height h of 38 mm, equivalent to an average slope of 4H:1V. The channel finally discharges to a stilling basin of 2.3 m in length. A unit flow q of 0.28 m^3/ms was used for data collection, and measuring points were defined on the channel central axis at the following abscissa (absc.): 0.00, 0.61, 1.22, 1.83, 3.05 m corresponding to the AIP, 3.66, 4.27 and 4.88 m.

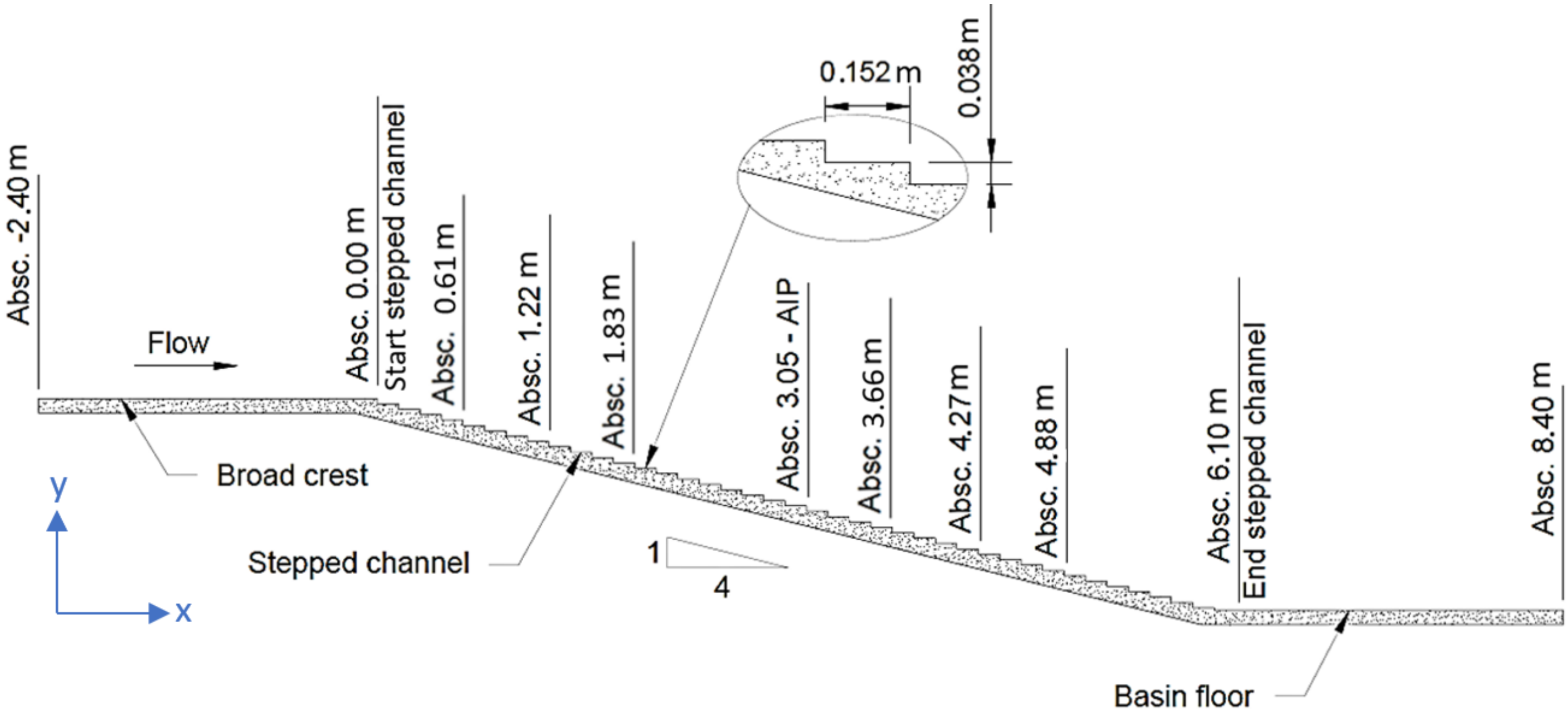

Figure 1. Geometry of the experimental stepped channel prototype. Source: Hunt and Kadavy (2010a, 2010b).

An Acoustic Doppler Velocimeter (ADV), a Pitot tube (PT) coupled to a differential pressure transducer, and a fiber optic (FO) probe were used to measure the instantaneous flow velocity. The use of the ADV was limited to a maximum velocity of 4.6 m/s (Hunt & Kadavy, 2010a), so it was employed upstream of the AIP. The PT did not have the ADV limitation, so it was used over the entire length of the channel. However, the main source of error in pressure measurement is the presence of high air concentrations in the flow (Matos, Frizell, André, & Frizell, 2002). The FO downstream of the 3.05 m abscissa was then used as a verification, since it works adequately in areas with a large air volume fraction.

Numerical model setup for validation

Models and equations

OpenFOAM software was used to solve the Reynolds-averaged Navier-Stokes (RANS) equations. The continuity and conservation of linear momentum equations for two-dimensional (2D) incompressible flow are Equation (1) and Equation (2), respectively:

$$\frac{\partial U_i}{\partial x_i} = 0 \tag{1}$$

$$\rho \frac{\partial U_i}{\partial t} + \rho U_j \frac{\partial U_i}{\partial x_j} = -\frac{\partial P}{\partial x_i} + \rho g_i + \frac{\partial}{\partial x_j}\left(\mu \frac{\partial U_i}{\partial x_j} - \rho \overline{u_i' u_j'}\right) \tag{2}$$

Where U_i is the mean flow velocity vector, subscripts $i, j = 1$ or 2 represent the two dimensions in space (x, y), x_i is the direction vector, t is the time, P is the static pressure of the mean flow, g_i is the gravity vector (0, -9. 81) m/s^2, ρ is the fluid density, μ is the dynamic viscosity, u_i' is the flow velocity vector for turbulent fluctuations, and $-\rho\overline{u_i' u_j'}$ is the Reynolds stress tensor. The flow can be considered two-dimensional if the stream width is greater than 5 to 10 times the height of the water depth (Sotelo-Ávila, 2002). Since the width of the stepped channel is approximately 18 times the average flow depth recorded in the experimental campaign, the 2D equations solved along the central plane between the sidewalls are adequate for the modeling process.

The turbulence model selected was RNG $k-\varepsilon$, which is derived from a mathematical technique called renormalization group (RNG). It applies the Boussinesq hypothesis for the turbulent viscosity (μ_T), such that the latter is assumed as a coefficient of proportionality between the Reynolds stress tensor and the velocity gradients of the mean flow. As in the standard $k-\varepsilon$ model, two additional equations are solved for the transport of the turbulent kinetic energy (k) and dissipation rate (ε), corresponding to Equation (3) and Equation (4), respectively:

$$\rho\frac{\partial k}{\partial t}+\rho U_j\frac{\partial k}{\partial x_j}=\frac{\partial}{\partial x_j}\left[\left(\mu+\frac{\mu_T}{\sigma_k}\right)\frac{\partial k}{\partial x_j}\right]+P_k-\rho\varepsilon \tag{3}$$

$$\rho\frac{\partial \varepsilon}{\partial t}+\rho U_j\frac{\partial \varepsilon}{\partial x_j}=\frac{\partial}{\partial x_j}\left[\left(\mu+\frac{\mu_T}{\sigma_\varepsilon}\right)\frac{\partial \varepsilon}{\partial x_j}\right]+C_{1\varepsilon}\frac{\varepsilon}{k}P_k-{R_\varepsilon}^{*} \tag{4}$$

Where $\sigma_k=\sigma_\varepsilon=0.71942$ are the effective Prandtl numbers for k and ε, respectively; P_k represents the production of k; $C_{1\varepsilon}=1.42$ is a constant derived analytically with the RNG theory, and ${R_\varepsilon}^{*}$ is an additional term with respect to the standard model, which improves performance in flows rapidly deformed and with streamline curvature (Escue & Cui, 2010).

These hydrodynamic phenomena are typical of recirculating vortices present in skimming flow, in the cavities between the tread and the riser of the steps, as well as in the main stream in the zone of impact with the final portion of the tread, just downstream of the vortex. The turbulent viscosity is calculated as $\mu_T=\rho C_\mu k^2/\varepsilon$, with the constant $C_\mu=0.0845$ also derived with RNG. For more detail regarding the equations and terms, the studies of Yakhot, Orszag, Thangam, Gatski and Speziale (1992), and Orszag, Yakhot, Flannery and Boysan (1993), who proposed the model are recommended.

For modeling the free surface of water, the volume of fluid (VOF) model proposed by Hirt and Nichols (1981) was applied, which adds an extra term (F_s) to Equation (2) to account for the surface tension at the water-air interface. In addition, ρ is replaced by the density of the mixture (ρ_m). F_s and ρ_m are presented in Equation (5) and Equation (6), respectively:

$$F_S = \int_{s'} \sigma k' n' \delta(x - x')\, ds' \tag{5}$$

$$\rho_m = \alpha \rho_l + (1 - \alpha)\rho_g \tag{6}$$

Where s' is the free surface, σ is the surface tension coefficient between water and air, k' is the curvature of the free surface, n' is the unit vector normal to the free surface, $\delta(x - x')$ is the Dirac delta function, where x is the coordinate at which the function is evaluated and x' is a point on the free surface to ensure that only there F_s is summed. The volume fraction of water α, is defined as the ratio of the cell volume (area in 2D) occupied by this liquid to its total volume, and ρ_l and ρ_g are the densities of the water and air phases, respectively.

Additionally, the transport Equation (7) is solved for α:

$$\frac{\partial \alpha}{\partial t} + U_j \frac{\partial \alpha}{\partial x_j} + \frac{\partial\left(U_{jc}\alpha(1-\alpha)\right)}{\partial x_j} = 0 \qquad (7)$$

Where the third term on the left-hand side of the equation has the function of compressing the free surface, since $\alpha(1-\alpha)$ ensures that it is only active in this region of the flow. The compression velocity vector (U_{jc}) in OpenFOAM, is bounded by the magnitude of the velocity vector on the cell faces $(|U_{jf}|)$, maximum in the flow field, and its direction is aligned with the vector normal to the interface (n_{jf}). Thus, it is guaranteed in Equation (8) (Cifani *et al*., 2016), that the compression term only introduces α transport in the direction normal to the free surface:

$$U_{jc} = \left[\min\left(C_\alpha |U_{jf}|, \left(|U_{jf}|\right)_{\max}\right)\right] n_{jf} \qquad (8)$$

Where C_α is a coefficient that defines the effect of the compression term. For values close to 0 a diffuse free surface is produced, and for values greater than 1 it is distorted, and numerical instability can be generated. In the present study $C_\alpha = 1$ was used.

For the solution of the equations, the *interFoam* solver with the PISO pressure-velocity coupling algorithm was used. In the latter, the continuity Equation (1) discretized by the finite volume method is adapted as a pressure equation to perform the momentum correction twice. For further details of the implementation of the PISO algorithm in OpenFOAM, the notes of Greenshields and Weller (2022) are recommended. The application of under-relaxation factors was not necessary.

Computational mesh and boundary conditions

Figure 2 shows the boundaries of the geometric domain of the model and the computational mesh used. The initial conditions (IC) and boundary conditions (BC) applied to the boundaries in Figure 2a are described below.

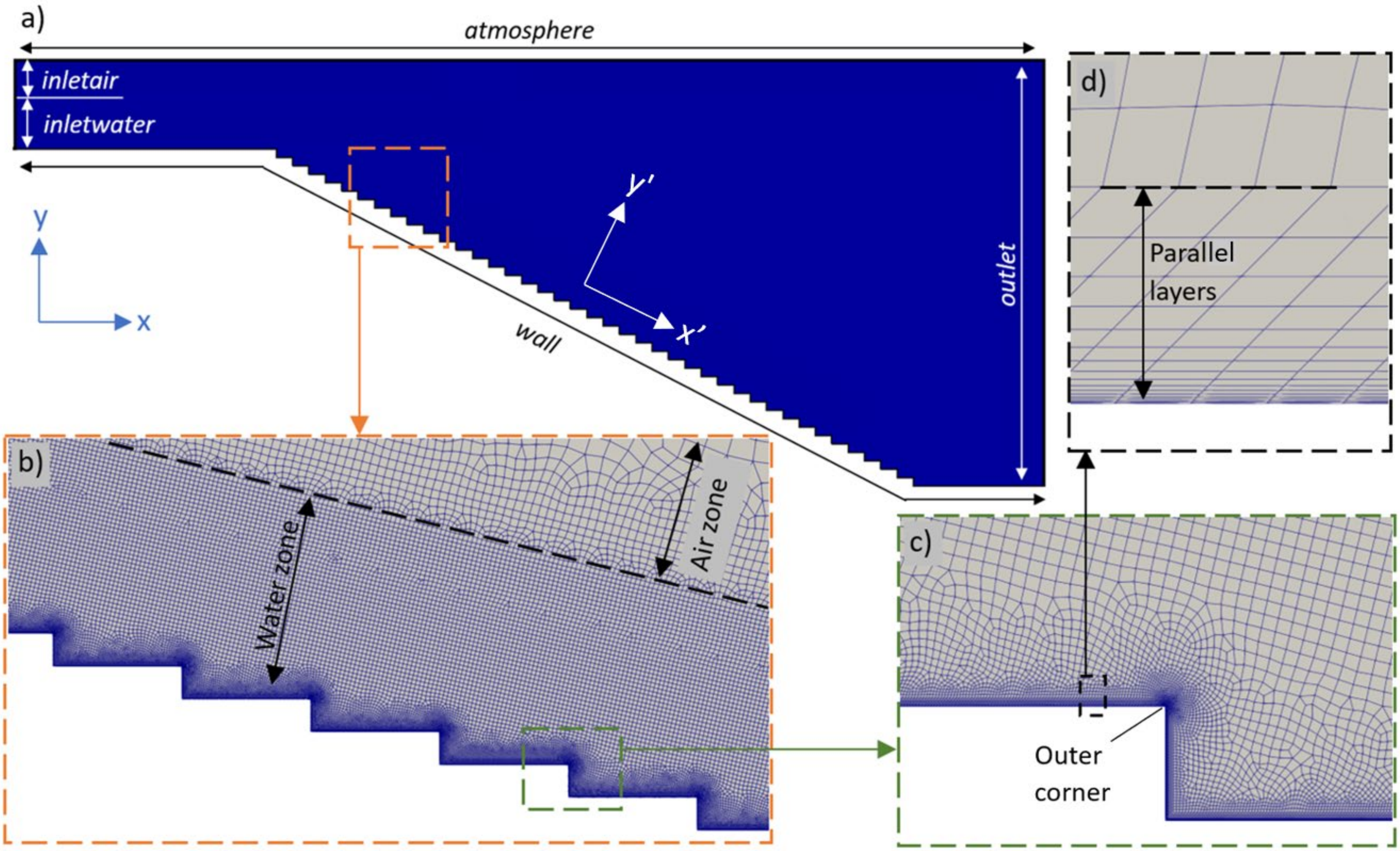

Figure 2. a) Boundaries and geometry of the numerical model for validation, b) computational mesh in the water zone and air zone, c) detail of the mesh in the steps, d) layers parallel to the bottom.

- **Velocity**: In *inletwater* a water inlet velocity vector of (1.21, 0) m/s is applied, which at the boundary height of 0.23 m produces the same experimental q of 0.28 m^3/ms. At *inletair* and *atmosphere* the *pressureInletOutletVelocity* BC, which is combined with *totalPressure* for pressure, was applied at atmospheric boundaries where inlet flow may be present, but its velocity is unknown. This BC specifies zero gradient for velocity (Greenshields, 2022). In outlet, the *inletOutlet* BC was defined which imposes zero gradient for outflow, and a velocity vector of (0, 0) m/s for inflow. For *wall*, the *noSlip* BC was used, guaranteeing zero velocity at the step bottom. The IC defined a velocity vector (0, 0) m/s throughout the internal domain.

- **Pressure**: In *inletwater*, *outlet* and *wall*, *fixedFluxPressure* BC was defined, which is equivalent to zero gradient, but adjusts the pressure gradient such that the flow at the boundary matches the velocity BC. It is useful in cases where the solution equations include gravitational and surface tension forces (Greenshields, 2022). The *inletair* and *atmosphere* boundaries were calculated with the *totalPressure* BC, such that for outflow the gauge pressure is atmospheric (p_o) equal to 0Pa, and for inflow it is $p_o - 0.5\rho {U_n}^2$, where U_n is the magnitude of the normal inlet velocity (tangential velocity is not considered). For IC, p_o was assumed throughout the internal domain.
- **Turbulence**: In inletwater the values of k and ε were defined with the approximations of Equation (9) (Versteeg & Malalasekera, 2007):

$$k = \frac{3}{2}\left(U_{ref}T_i\right)^2, \varepsilon = 0.09^{3/4}\frac{k^{3/2}}{l}, l = 0.07L \tag{9}$$

Where U_{ref} is the magnitude of the velocity at the boundary, T_i is the turbulence intensity assumed to be 3 %, l is the turbulent length scale, assumed to be a function of the characteristic length at the channel entrance (L). Results k of 0.002 m^2/s^2 and ε of 0.0009 m^2/s^3 were obtained. In *wall* the *epsilonWallFunction* BC was set for ε, which determines the dissipation value depending on the dimensionless distance to the first cell (y^+). If $y^+ < 11$ the deductions for the viscous sublayer are used, and if $y^+ > 11$ those for the inertial sublayer which behaves based on the law of logarithms. The boundary value of 11, results from the intersection of the velocity profiles in both regions of the boundary layer (Greenshields & Weller, 2022). For the calculation of y^+ and ε in OpenFOAM, Equation (10) was used:

$$y^+ = C_\mu{}^{1/4} \frac{k^{1/2} y_w}{\nu}, \varepsilon = \varepsilon_{vis} = \frac{2\nu k}{y_w{}^2} \tag{10}$$

Where y_w is the distance from the cell center to the wall, ν is the kinematic viscosity of the fluid, and ε_{vis} is the dissipation in the viscous sublayer. The expression for $y^+ > 11$ is not presented in this study, since as described below in the mesh description, the height of the first cell layer guaranteed a complete solution of the boundary layer. Therefore, the *nutkWallFunction* BC for μ_T, assumed a fixed value of zero since the mesh resolution guaranteed laminar flow near the wall. For k, the *kqRWallFunction* BC was applied, which is equivalent to zero gradient. For the rest of the boundaries, the *inletOutlet* BC was defined for k and ε, and for the IC the same results obtained for the inlet with Equation (9) were applied throughout the domain.

- **Water volume fraction**: In *inletwater* a value of α of 1 was defined. For the air boundaries the *inletOutlet* BC was defined with an inlet value of zero, and for the bottom the zero gradient BC. For the IC, α

of 0 was assumed for the entire domain, such that it was filled with air and the water was about to enter through *inletwater*.

The computational grid had two main regions: water zone and air zone (Figure 2b). The first one had a higher resolution since it included the main stream flow over the steps, as well as the free surface. The second only models the atmospheric airflows, so it was generated with lower resolution, the latter increasing only near the boundary with the water zone. In the steps, at a shorter distance from the wall, the magnitude of the cells was gradually reduced, increasing the resolution at the outer corners because these are the points with the greatest gradients (Figure 2c). In the region adjacent to the wall boundary and parallel to its geometry, layers of cells with a growth factor of 1.3 (height ratio between two subsequent layers) were generated in order to capture the flow phenomena in the viscous sublayer and in the transition region to the inertial sublayer (Figure 2d).

To establish the resolutions, a sensitivity analysis was initially performed with three grids. The main characteristics that differentiate them are presented in Table 1. The resolution in the water zone refers to the average size of the cell faces away from the steps (it does not consider the increase in resolution near the wall), and y^+ average and maximum resulted from analyzing the dimensionless distances of all the cells in the first parallel layer, adjacent to the *wall* boundary and whose height is also included in Table 1. The value of the average numerical error with respect to the experimental data $E\_prom.$, at absc. 0.00, 0.61, 1.22 and 1.83 m, was calculated with Equation (11):

$$E\_prom\,(\%) = \frac{100}{N}\sum_{n=1}^{N}\left[\frac{\left(U_{x'-RNG\,k-\varepsilon}\right)_n - \left(U_{x'-exp}\right)_n}{\left(U_{x'-exp}\right)_n}\right] \qquad (11)$$

Where n are the measurement points on each abscissa, increasing in the y' direction perpendicular to the pseudo-bottom (see axes in Figure 2a) up to the farthest point from the wall (N); $U_{x'-RNG\,k-\varepsilon}$ is the flow velocity calculated by the numerical model with $RNG\ k-\varepsilon$ for turbulence, and $U_{x'-exp}$ the measured in the experimental campaign with TP, ADV and FO, all in the x' direction.

Only the absc. in the non-aerated zone were analyzed since the numerical model did not capture the air insertion downstream of the AIP. In this study, it is considered that the selection of the mesh should be based on the analysis of the results compared to the experimental measurements, in the zone where the numerical model is able to faithfully capture the characteristics of the skimming flow.

Table 1. Mesh sensitivity analysis of the numerical model for validation.

Mesh	**Total number of cells**	**Water zone resolution (m)**	**First parallel layer Height (m)**	y^+ **average**	y^+ **maximum**	E_prom **absc. 0.00 m (%)**	E_prom **absc. 0.61 m (%)**	E_prom **absc. 1.22 m (%)**	E_prom **absc. 1.83 m (%)**
Mesh 1	500 241	5.00E-03	1.00E-05	0.4	1.9	1.4	3.9	3.9	5.0
Mesh 2	191 531	7.00E-03	5.00E-05	1.8	5.2	2.0	4.2	3.7	5.1
Mesh 3	125 822	9.00E-03	1.00E-04	3.6	8.7	2.0	4.4	3.8	5.2

The average errors obtained show that, in all three cases, the numerical results are independent of the mesh resolution. The main difference occurs at absc. 0.00 m for mesh 1 with respect to 2 and 3, but as the flow advances towards the AIP, E_prom becomes approximately the same for all three meshes. Figure 3a presents the numerical velocity profiles at absc. 1.83 m, along with the PT measurements. In Figure 3b and c, the behavior of the three computational resolutions can be observed at an enlarged scale, in the areas enclosed by the panels shown in Figure 3a. Near the stepped bottom (Figure 3b) the numerical model underestimates the flow velocity, and the difference with respect to the measurements is smaller for the finer mesh. Farther away from the wall, in the main stream velocity gradient zone (Figure 3c), the numerical model velocity is higher than the experimental one, and contrary to what is shown near the pseudo-bottom, the difference is higher for mesh 1.

Closer to the free surface, outside the boundary layer, the three meshes converge to the same result. Finally, it can be stated that, although in most absc. a lower E_prom was obtained for the higher resolution mesh, there is no considerable difference between the three numerical results. This behavior is similar in the other upstream abscissa, therefore, it is not worth including them in Figure 3.

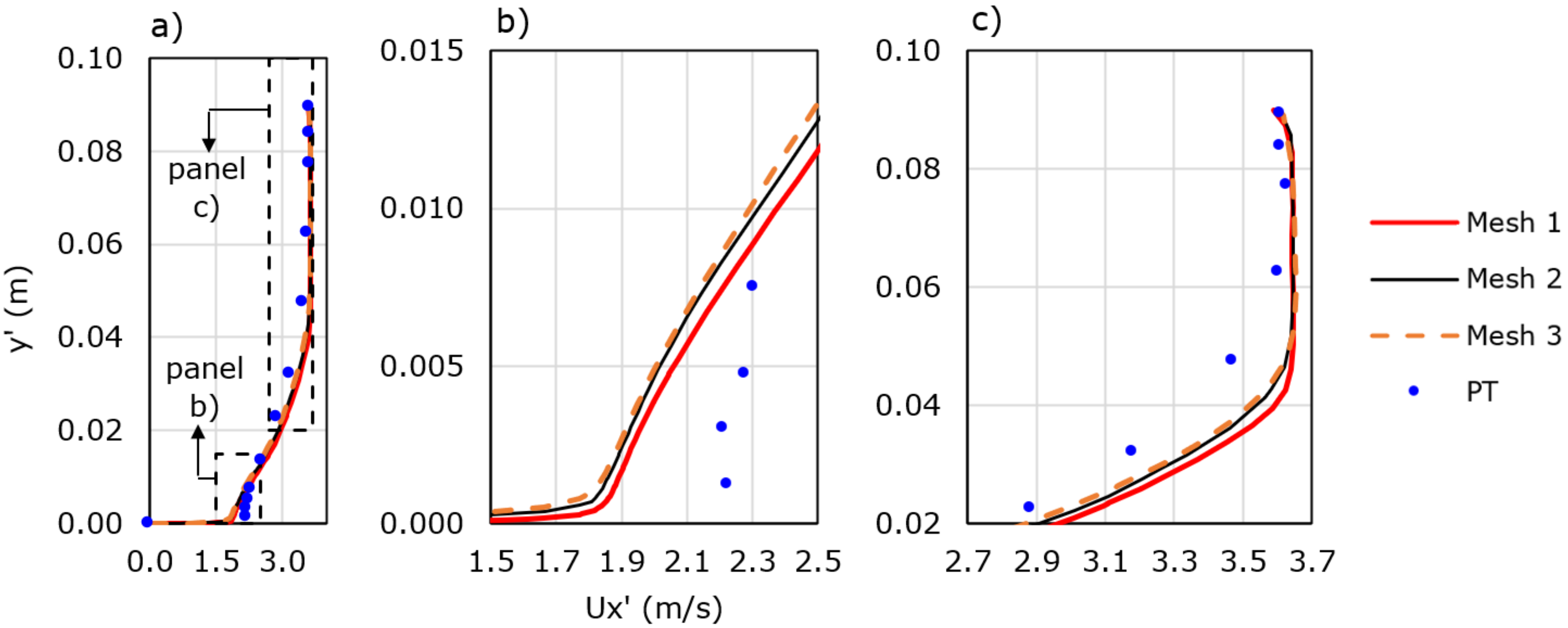

Figure 3. a) Experimental and numerical velocity profiles for the three meshes at absc. 1.83 m, b) detail of the velocity profile near the bottom, c) detail of the velocity profile in the main stream.

Due to the discussion above, the mesh selection is not based on E_prom, but on the average and maximum y^+ values. To obtain a complete modeling of the boundary layer, the mesh must have cells thin enough near the wall to resolve the flow in the viscous sublayer (region bounded by $y^+ < 5$). For the above, a $y^+ \sim 1$ is recommended in the first layer (Greenshields & Weller, 2022). Although the average value in meshes 2 and 3 is within the laminar flow region, the maximum value is not. Consequently, it can be stated that part of the boundary with the steps lies in the transition region to the logarithmic zone (region bounded by $5 < y^+ < 30$), where both viscous and Reynolds stresses are important

(Versteeg & Malalasekera, 2007). Only mesh 1 can guarantee the solution of the viscous sublayer on the entire *wall* boundary (average y^+ and maximum < 5), so it was selected for the runs in the present paper.

Configuration of the numerical model for the stepped channel with vertical curves

Based on the validation of the numerical model with the experimental data of Hunt and Kadavy (2010a, 2010b), an additional model in a stepped channel with vertical curves was run. The same turbulence and multiphase flow model were used: RNG $k - \varepsilon$ and VOF, respectively. Figure 4 presents the geometrical parameters of the channel. The total vertical fall remained approximately 1.5 m, but the average slope of the straight section was increased (1H:1V), with steps having both h and l equal to 38 mm. This increase was to obtain pseudo-bottom curves with smaller radius and to be able to adjust the geometry of the steps to them. For this purpose, they were defined with constant h also of 38 mm, and variable l extending each tread to intercept the curve. The steps A, B and C in curve 1 (convex), and their corresponding geometry G, F and E, respectively, in curve 2 (concave) were selected for further analysis in the results section. D in the straight section was identified for comparison with the area without curves.

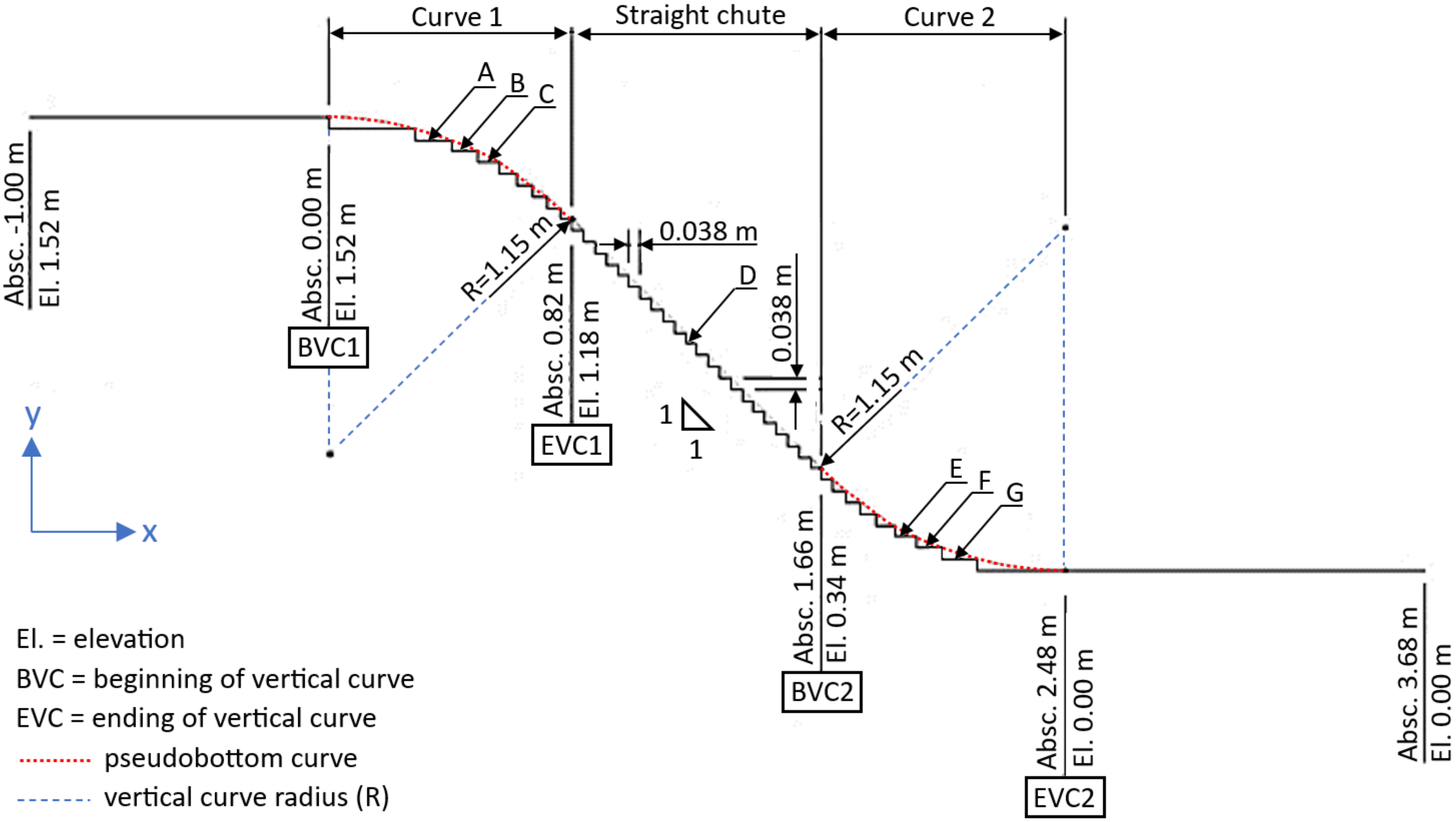

Figure 4. Stepped channel geometry with vertical curves.

For the design of the convex pseudo-bottom curve, the Bureau of Reclamation (1987) recommends that the bottom describe a shape slightly flatter than that of the free jet trajectory, launched with a head equal to the specific energy of the stream initiating the curve. For the geometry, it proposes Equation (12):

$$-y = x\tan\theta + \frac{x^2}{K[4(d+h_v)\cos^2\theta]} \tag{12}$$

Where θ is the angle of inclination of the channel bottom upstream of the curve, K is a factor that must be equal to or greater than 1.5 to ensure positive pressures distributed over the entire contact surface of the curve, avoiding flow separation, h_v is the velocity head and d is the depth of flow in the BVC. For the concave curve, the design recommendation is based on a radius sufficient to minimize the dynamic forces produced at the bottom by the change in flow direction. Radii greater than or equal to five times the flow depth are considered acceptable (Bureau of Reclamation, 1987). $R = 1.15m$ was selected (Figure 4), based on the maximum depth of flow at the channel entrance (0.23 m), complying with the recommendation for curve 2, and approaching the trajectory described by Equation (12) for curve 1.

Figure 5a shows the boundaries of the geometric domain of the model. The IC and BC applied to the boundaries were the same as those validated in the previous model. The computational mesh presented in Figure 5b-d was also generated based on the same parameters used for the validation model. A total number of cells of 393 239 was obtained, keeping the same resolution in the water zone of 5.00E-03 m. Although $q = 0.28m^3/ms$ is the same, the flow velocity and the shear stress in the wall increase, due to the higher slope in the stepped channel with curves. Therefore, it was necessary to decrease the height of the first parallel layer: 5.00E-06 m, to guarantee the modeling of the viscous sublayer (average and maximum y^+ of 0.2 and 1.3, respectively).

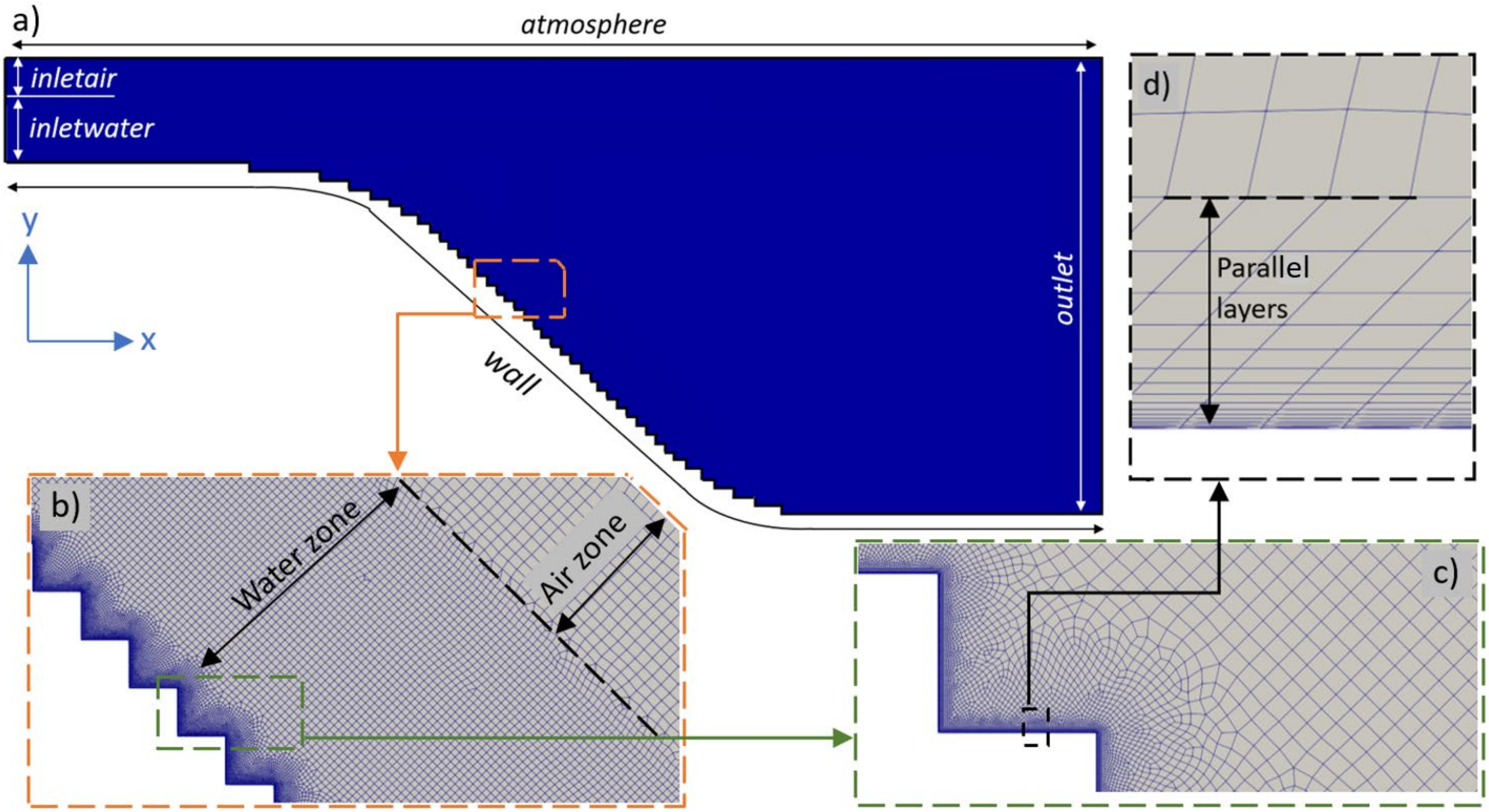

Figure 5. a) Boundaries and geometry of the numerical model with vertical curves, b) computational mesh in the water zone and air zone, c) detail of the mesh in the steps, d) layers parallel to the bottom.

Results and discussion

The results below correspond to the final steady flow condition. This is reached time after the flow leaves the *outlet* boundary, enough for the hydrodynamic variables to stabilize.

Numerical model validation

Figures 6a and 6b present the numerical velocity profiles with the RNG $k-\varepsilon$ turbulence model, upstream and downstream of the AIP, respectively, together with the measurements with PT, ADV and FO. In general, at absc. upstream of the AIP a good fit of the numerical data to the experimental one is observed. At abscissa 0.00 m the numerical model manages to capture the shape and magnitude of the mean flow velocity profile, over the entire distance y'. Between absc. 0.61 and 3.05 m, near the bottom, for values of y' less than about 0.01 m (26 % of h), the numerical results underestimate the experimental data. Far from the bottom, in the low velocity gradient zones (outside the boundary layer), the fit is satisfactory at all stations. However, at absc. 3.05 m, velocity gradient is observed for the first time over the entire y' range, indicating the interception of the boundary layer with the free surface. This agrees with the AIP experimental report. Similar to that shown in Figure 6a and Table 1, Bombardelli *et al.* (2011) also obtained an increase in numerical error with respect to the measurements as the flow approached the AIP, reporting an E_prom of 7 %. The fit in the present study is slightly better, obtaining a maximum E_prom of 5 % in the non-aerated flow zone.

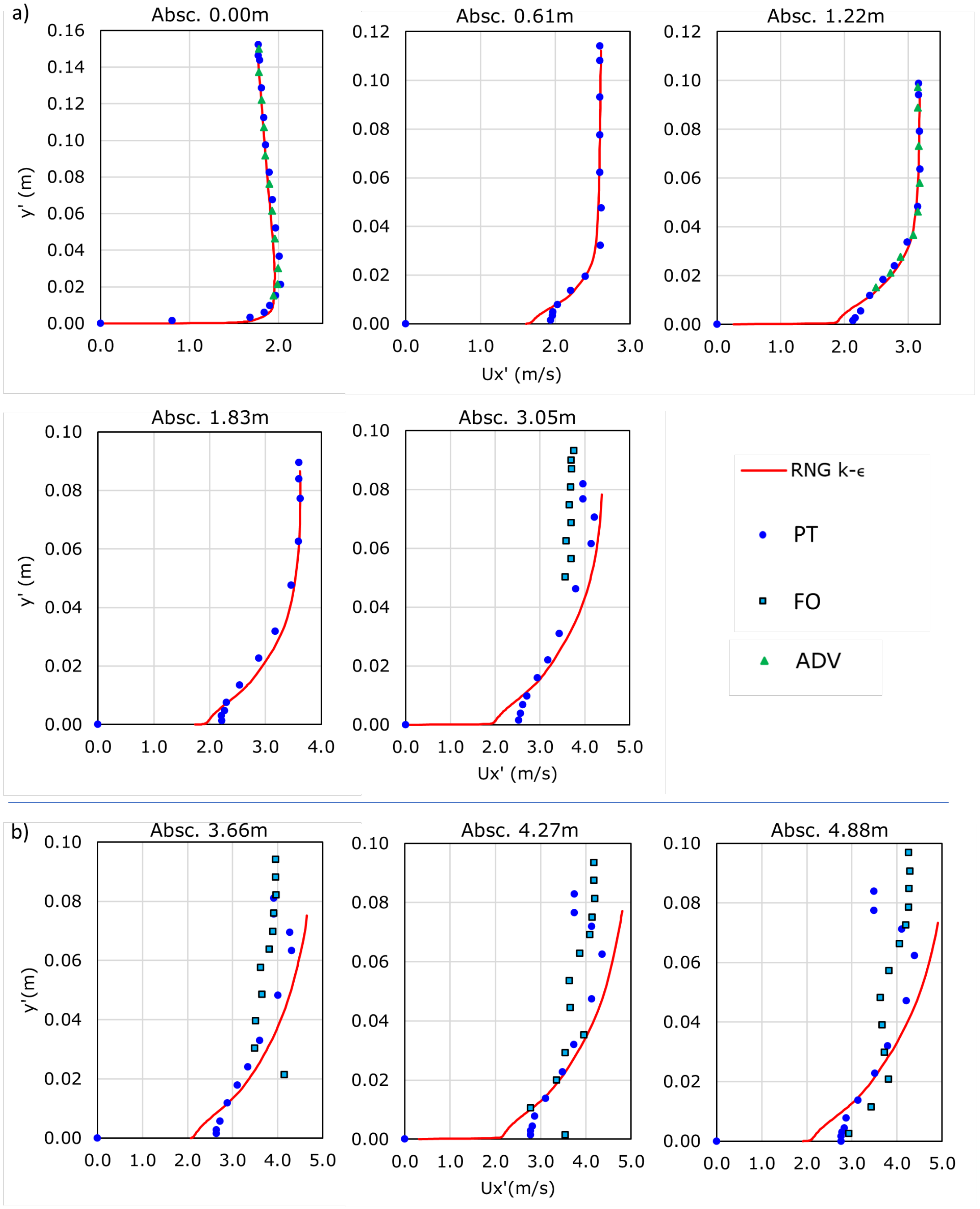

Figure 6. Validation of mean flow velocity profiles for a unit flow rate of 0.28 m³/ms, at a) absc. upstream of the AIP, b) absc. downstream of the AIP. Experimental data source: Hunt and Kadavy (2010a, 2010b).

In the aerated flow zone, although the numerical profiles capture the shape of the experimental ones, the quality of the fit continues to decrease in the flow direction. For y'<0.01 m, the greater the distance downstream, the greater the underestimation of the measurements, and for y'>0.01 m, the greater the overestimation of the numerical velocity relative to the experimental one. This overestimation and lower quality of fit was also reported by Cheng, Luo, Zhao, and Li (2004), who used the standard $k-\varepsilon$ turbulence model. The higher error downstream of the AIP is because the numerical runs did not capture the aeration of the flow in that region. This can be verified for both the numerical validation model and the vertical curves model in Figure 7, which presents the variation of α in space. Note that, for water flow between the *inletwater* and *outlet* boundaries, $\alpha = 1$ throughout the entire domain. Similar results for α were reported by Medhi *et al.* (2019).

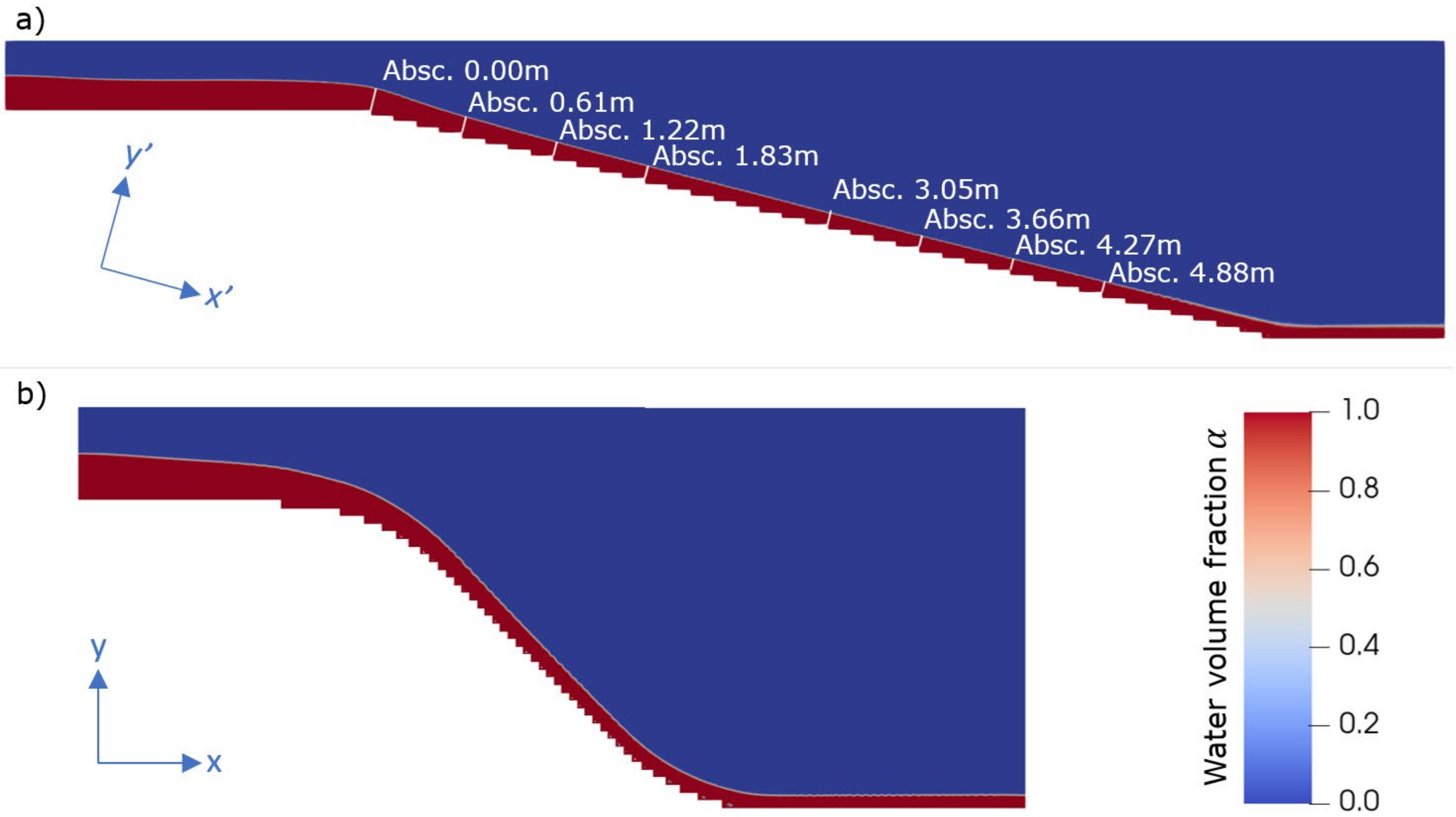

Figure 7. Water volume fraction α in a) numerical model for validation, b) numerical model with vertical curves.

The difficulty in capturing the flow aeration phenomenon was reported by Casa, Hidalgo, Castro, Ortega, and Vera (2018), who applied an air incorporation sub-model using Flow-3D software. When a disturbance of magnitude equal to the turbulent length scale at the free surface is associated with a turbulent kinetic energy per unit volume P_t, greater than the energy associated with the stabilizing forces of gravity and surface tension P_d, the sub-model allows the inflow of a volume of air

(Hirt, 2003). However, the results of Casa *et al*. (2018) for the flow depth in the aerated region, also using VOF and RNG $k-\varepsilon$, showed a large dependence on the grid resolution, and errors that increased to more than 100 % with respect to the experimental information, as the cell size decreased.

In large eddy simulation (LES), the larger structures are solved directly while the smaller ones are modeled. It is based on the idea that momentum, mass, and energy are mainly transported by the larger eddies, which vary depending on the geometry and boundary conditions of the flow under analysis. Small eddies on the other hand, tend to be more isotropic and universal (Ansys Inc., 2022). By not applying the time filter typical of Reynolds-averaged models, such as the RNG $k-\varepsilon$ of the present study, the velocity fluctuations of the larger scale flow structures are obtained, resulting in several advantages for modeling the skimming flow. For example, it allows capturing turbulence anisotropy (which is not possible with the Boussinesq hypothesis), thus better predicting flows with sudden changes in mean strain rate, with boundary layer separation, flows over curved surfaces, rotating fluids, and three-dimensional flows (Wilcox, 2006). All the above, typical characteristics in stepped channels with vertical curves. In addition, the results obtained by Zhan, Zhang, and Gong (2016) for modeling the skimming flow using the Eulerian model of Chahed, Roig, and Masbernat (2003) for multiphase flow, combined with RNG $k-\varepsilon$, showed similar results to those in Figure 7. However, when using LES for turbulence, a qualitative inspection of the animation in Appendix A of that reference, allows observing how the instantaneous fluctuations in the free surface contribute to air trapping, a phenomenon suppressed by Reynolds averaging in Figure 7. The comparison of the numerical profiles of α with the experimental ones, showed satisfactory results. Therefore, within the plans for future research, the working group of this paper intends to analyze vertical step curves in the aerated region using LES.

Another detail to note in Figures 6a and 6b is that from abscissa 1.83 m downstream including the aerated flow, the experimental data with PT show near the bottom an approximately constant velocity. This behavior has been previously reported experimentally by Boes and Hager (2003), and Gonzalez (2005), and numerically for the non-aerated region by Bombardelli *et al.* (2011). However, the numerical modeling in the present study does not capture it adequately despite applying a complete modeling of the boundary layer. This behavior may be associated with an underestimation of μ_T in the RNG $k-\varepsilon$ model, which limits the turbulent transport of flow with higher momentum from areas farther from the wall towards the stepped bottom, causing an underestimation of the velocity. Yet, Bombardelli *et al*. (2011) despite using the same turbulence model, reported the opposite phenomenon: velocity overestimation. The simplification of the flow to a 2D condition, and of the turbulence to a Reynolds-averaged condition, may also influence by not capturing the three-dimensional flow structures, nor the influence of the Reynolds stress tensor anisotropy (see the difference in the recirculating structures of the flow, captured using a LES vs. a RANS model by Zhan *et al.* (2016)). Further research is recommended to provide clarity in this regard.

Pressure and turbulent dissipation rate in the channel with stepped vertical curves

By applying Prandtl's simplification to Equation (2) for x momentum component, for near-bottom flow, the advective term is assumed to be zero (since $U_x \approx U_y \approx 0$), and $\rho\overline{u_i'u_j'}$ as well since turbulent stresses in this zone are negligible (Kundu, Cohen, & Dowling, 2012). Equation (13) is then obtained:

$$\left(\frac{\partial P}{\partial x}\right)_{pared} = \mu\left(\frac{\partial^2 U_x}{\partial y^2}\right)_{pared} \tag{13}$$

Where $(\partial P/\partial x)_{wall}$ is the pressure gradient in the x-direction over the tread of the steps, and $\mu(\partial^2 U_x/\partial y^2)_{wall}$ is the curvature of the mean flow velocity profile (U_x vs. y) near the wall. The left-hand term plays an important role in the direction of flow near the bottom and the occurrence of the boundary layer separation phenomenon, allowing to analyze the two main zones in the steps: flow separation and reattachment. The velocity vectors in these two zones are illustrated in Figure 8a for step G in the concave curve and are colored as a function of the ratio between the velocity magnitude (U) and the maximum velocity in the entire channel (Umax). Figure 8c plots the variation of U_x normalized by the maximum positive velocity at x in the step (U_{x-max}), along the x_l/l axis. The latter represents the tread length fraction and is calculated as the ratio between the horizontal distance to the riser (x_l), and the total length of the tread. The separation zone is composed in the initial section of a small recirculation vortex (SRV) shown in detail in Figure 8b. There, U_x/U_{x-max} is positive at the bottom (see zoom in Figure 8c), and then there is a large vortex (BRV) with negative U_x/U_{x-max}. The reattachment zone starts just downstream of the flow reattachment point (RP), where the main stream impacts with the tread and continues downstream in the same direction as the x_l/l axis.

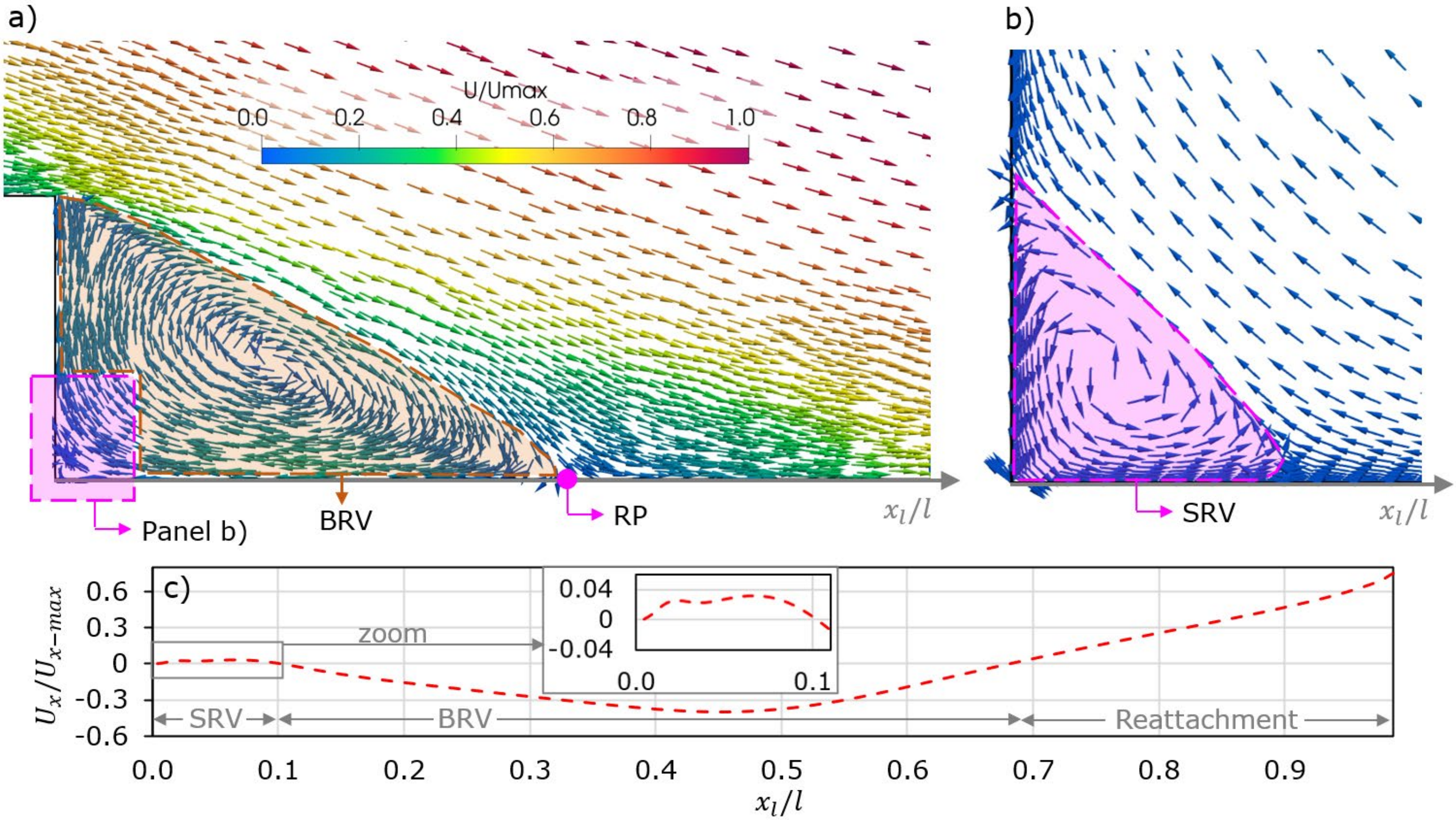

Figure 8. a) Flow velocity vectors, b) SRV detail, c) U_x/U_{x-max} along the tread at a distance from the bottom of 2.50E-06 m. Results corresponding to step G.

Velocities in the separation zone are the lowest, corresponding to less than 20 % of Umax, and in the reattachment zone they are higher, increasing to 40 %. The maximum flow velocities occur above the pseudo-bottom in the main stream (> 40 % of Umax), like the results of Arjenaki and Sanayei (2020) for a 3D step channel modeled also with RNG $k-\varepsilon$.

The existence of the separation and reattachment zones was previously discussed by Chanson (1994) and Llano (2003), who identified three skimming flow sub-regimes. The SK1 for $h/l < 0.27$, in which the outer boundary of the BRV impacts on the intermediate zone of the tread, and which corresponds to the one shown in Figure 8. The SK2 for $0.27 < h/l < 0.47$, in which the recirculation vortices of adjacent steps interact with each other, fully occupying the treads (the reattachment zones disappear). Finally, SK3 for $h/l > 0.47$, in which the separation zone is composed of more stable vortices, also occupying the entire step, but not interacting with the flow of neighboring steps. The results in Figure 8 agree with the velocity vectors reported by Medhi *et al*. (2019) for the BRV, however, they do not report the SRV. Figure 8a shows the proximity of the latter to the wall, so the mesh resolution near the step, $y^{+} \sim 1$ in this study vs. $30 < y^{+} < 300$ in that of Medhi *et al.* (2019), is a possible explanation for the numerical conditions needed to capture it. Wang, Wu, and Zhu (2019) showed the existence of this vortex experimentally by particle image velocimetry (PIV) and found a good numerical fit with direct numerical simulation and LES, but a smaller vortex with $k-\varepsilon$. Therefore, the selected turbulence model may also influence the proper representation and capture of this flow phenomenon.

For the totality of the selected steps (A-G in Figure 4), Figures 9a and 9b show the variation of $(\partial P/\partial x)_{wall}$, and of the turbulent kinetic energy dissipation rate (ε_{wall}), respectively, along x_l/l. The above, to analyze the fraction of the steps occupied by the vortex vs. the reattachment flow, and the difference in the dissipation distribution in those regions, emphasizing the comparison of those characteristics between the convex curve, the straight section, and the concave curve. In Figure 9a, for the smallest values of x_l/l, a first favorable pressure gradient ($(\partial P/\partial x)_{wall} < 0$), identified as the small vortex influence zone (SRV-IZ), is observed. The positive direction of flow in the tread with respect to the x_l/l axis, which causes the SRV to rotate counterclockwise (see Figure 8b), is due to the sign of the pressure gradient and extends from the riser to approximately the minimum $(\partial P/\partial x)_{wall}$ point in the SRV-IZ. For reference note that, for G this is at $x_l/l \approx 0.1$, a value up to which U_x/U_{x-max} is positive in Figure 8c. Downstream, the remaining part of the favorable gradient is responsible for decreasing the flow velocity near the bottom of the BRV, in the negative x_l/l direction. The adverse pressure gradient ($(\partial P/\partial x)_{wall} > 0$) is located in the middle region of the tread, identified as the big vortex influence zone (BRV-IZ). The sign of the pressure gradient produces a flow direction at the wall opposite to the x_l/l axis, and the consequent clockwise rotation of the BRV.

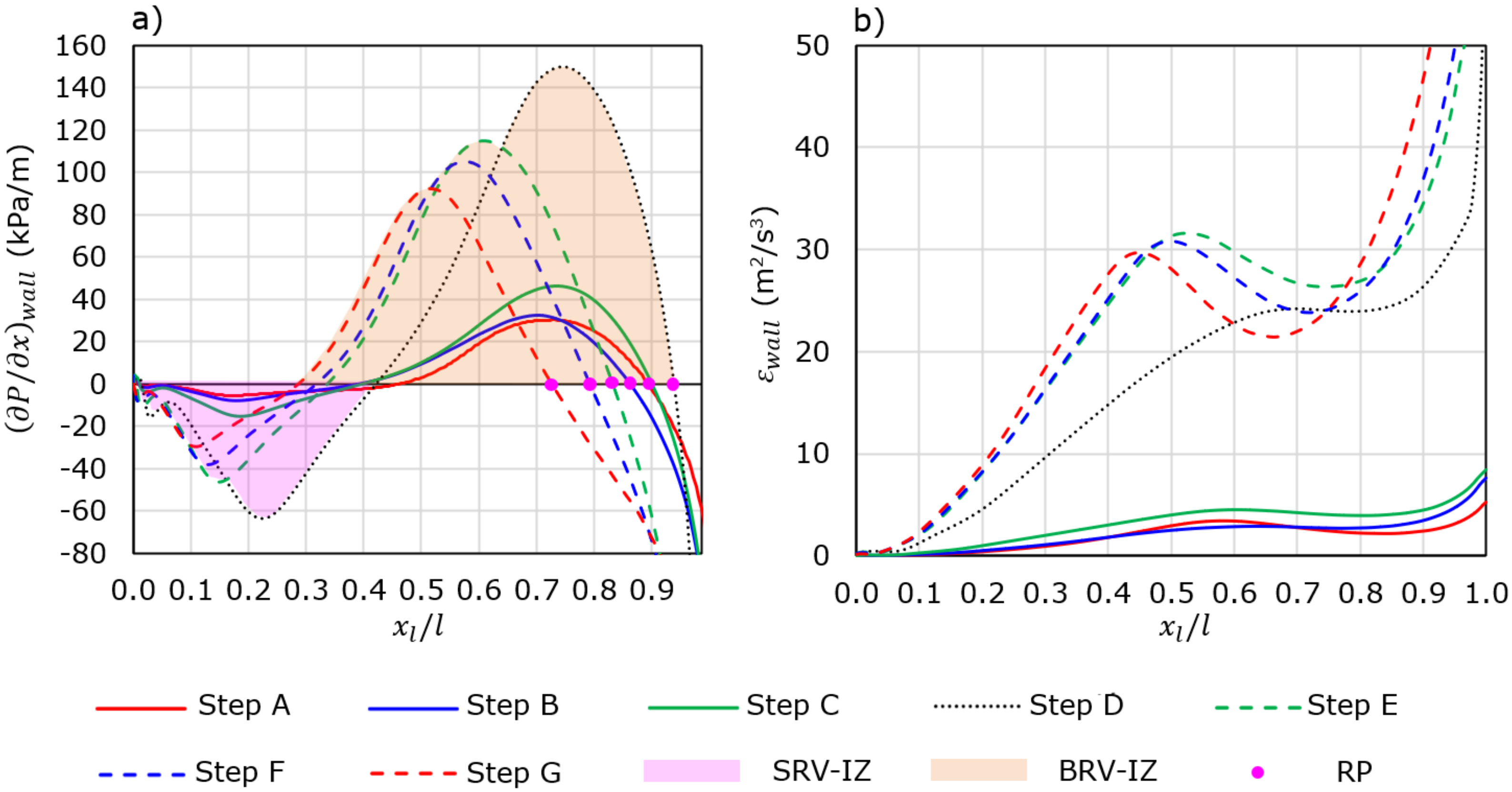

Figure 9. Variation along the tread of a) pressure gradient, b) dissipation. Convex curve (steps A, B, and C), straight section (step D), and concave curve (steps E, F, and G).

The SRV-IZ and the BRV-IZ together, form the flow separation zone, which extends approximately until $\partial P/\partial x_{wall}$crosses the x_l/l axis for the second time in the RP. For reference note that, for G this is at $x_l/l \approx 0.7$, the value at which effectively U_x/U_{x-max} becomes zero in Figure 8c. The change of the gradient from adverse to favorable produces a flow stagnation point, and the beginning of the reattachment zone that goes up to $x_l/l = 1$. The results in Figure 9a agree with those of Zhan *et al.*

(2016) and Saqib *et al.* (2022), who also found decreasing pressure values in the x_l/l direction at both ends of the tread and increasing ones in the intermediate zone. The former authors, as well as in the present study, associated the point of maximum pressure in the tread (which coincides with the second time $(\partial P/\partial x)_{wall}$ crosses x_l/l axis), with the approximate location of the RP.

Table 2 presents a comparative analysis of the occupancy of the steps in the vertical curves and in the straight section, by the vortices of the separation zone, and by the reattachment zone.

Table 2. Comparative analysis of the flow separation and reattachment zones in the vertical curves and the straight section.

Steps A, B, and C (convex curve region)	**Step D (straight section region)**	**Steps E, F, and G (concave curve region)**
	Flow separation zone	
The minimum and maximum values of $(\partial P/\partial x)_{wall}$, increase in the flow direction (A→B→C). Moreover, they are the smallest with respect to the other two regions	Zone with the largest minimum and maximum values of $(\partial P/\partial x)_{wall}$	The minimum and maximum values of $(\partial P/\partial x)_{wall}$, decrease in the flow direction (E→F→G). The magnitudes are intermediate with respect to the other two regions
Approximately 15 to 20 % of the tread is occupied by the SRV. Its occupancy increases in the direction A→B→C	A little more than 20 % of the tread is occupied by the SRV. It occupies a larger fraction than in the vertical curves	Approximately 10 to 15 % of the tread is occupied by the SRV (less than in the other two regions). Its occupancy decreases in the E→F→G direction
The RP is located at approximately 85 to 90 % of the tread. In the A→B→C direction, the relative distance to the riser, x_l/l, appears to vary randomly	The RP is approximately located at 95 % of the tread. x_l/l is larger than in the vertical curves	The RP is approximately located at 70 % to just over 80 % of the tread. x_l/l is the smallest with respect to the other two regions, approaching the riser in the E→F→G direction
	Flow reattachment zone	
It occupies approximately 10 to 15 % of the tread	It occupies approximately 5 % of the tread. Its occupancy is the lowest	It occupies approximately 20 to 30 % of the tread. Its occupancy is the highest

Step D with h/l of 1, corresponds according to Llano (2003) to a SK3 subregime. This agrees with deductions presented in Table 2, since the separation zone occupies approximately the entire tread, but without interfering with the vortex of the subsequent step. The h/l ratio of the steps in the convex curve: A, B, and C, is 0.32, 0.43 and 0.53, respectively, equal to that of the corresponding steps in the concave curve: G, F and E. According to Llano (2003) they correspond to subregimes SK2 and SK3. However, the numerical results correspond to an SK1, with a clearly differentiated reattachment zone. It is shown that the ranges of the subregimes originally proposed in the literature for straight sections are affected in vertical curves by the shape of the streamlines. In the concave curve, the dynamic forces produced at the bottom by the reduction of the slope compress the separation zone progressively, from step to step in the E→F→G direction, generating the lowest fractions of the BRV and the SRV occupancy. The opposite effect occurs in the convex curve in which the streamlines tend to move away from the bottom, producing a higher occupancy of the separation zone and its vortices.

The behavior of the streamlines also affects the turbulent dissipation rate. Figure 9b shows that their distribution along the tread is smaller in the convex curve and increases downstream as the flow exerts greater dynamic forces on the steps (it is greater in the straight section and finally maximum in the concave curve). The dissipation of energy in the flow is associated with the separation and reattachment zones. The vortices in the former are maintained by the transfer of turbulent shear stresses from the stream over the pseudo-bottom and are primarily responsible for extracting energy from the flow. In the latter, friction of the reattached flow with the wall generates energy dissipation (Chanson, 1994). The distributions of ε_{wall}in Figure 9b agree with this. All curves start at a minimum value in the zone of the SRV that does not contribute to dissipation, and grow in the direction of the x_l/l axis up to a first maximum whose location coincides approximately with that of the maximum adverse pressure gradient (Figure 9a), in the intermediate region of the BRV. Finally, for the value of x_l/l corresponding to the RP, ε_{wall} starts to grow at a higher rate, and at the step edge it reaches the maximum values in the whole tread. This shows that near the bottom the highest turbulent dissipation occurs in the reattachment zone.

Ashoor and Riazi (2019) found similar results for the comparison of a concave and a convex step channel. They associated the higher dissipation in the former only with the recirculation vortices. In this regard, although in the present study it is also obtained that the BRVs with higher ε_{wall} are those of the concave curve, the contribution of the maximum dissipation due to the friction with the bottom in the final section of the treads is also highlighted. Note that in the E→F→G direction, maximum ε_{wall} in the BRV decreases, while in the reattachment zone the dissipation increases step by step.

To complete the analysis of the distribution of the variables along the tread, profiles in sections perpendicular to the tread are presented below. The steps A and G of equal geometry in curves 1 and 2 are selected for comparison. In these, perpendicular section 1 ($S1$) is located at x_l/l of the minimum $\partial P/\partial x_{wall}$ in the SRV-IZ, section 2 ($S2$) in x_l/l of the maximum $\partial P/\partial x_{wall}$ at the BRV-IZ, and section 3 ($S3$) in x_l/l corresponding to the second crossing of $\partial P/\partial x_{wall}$ (approximately at the RP). Figures 10a, 10b, and 10c show the velocity, pressure and dissipation magnitude profiles at $S1$, $S2$ and $S3$, respectively.

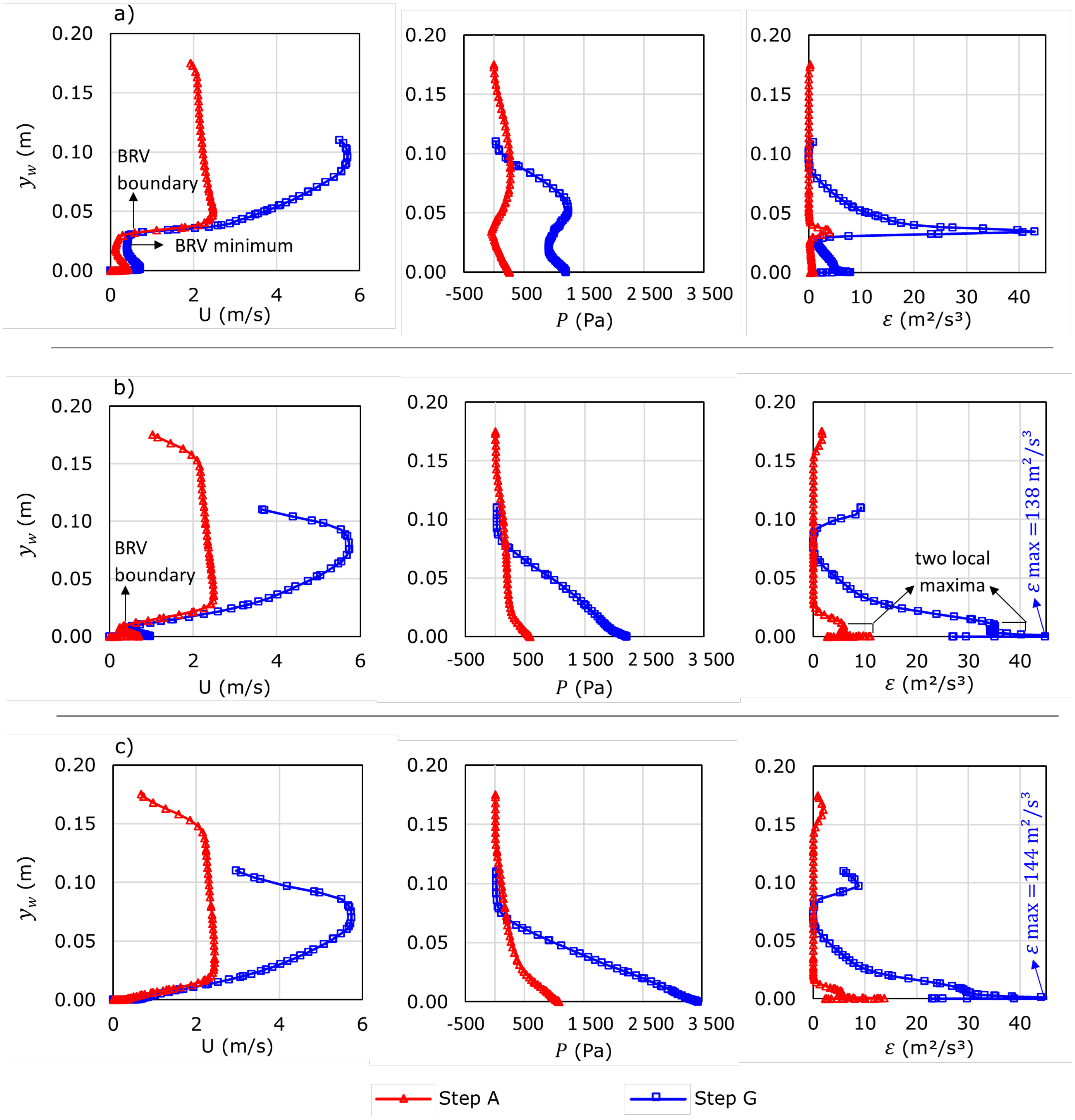

Figure 10. Comparison between the convex curve (step A) and the concave curve (step G) of velocity magnitude, static pressure, and dissipation rate profiles at a) $\boldsymbol{S1}$, b) $\boldsymbol{S2}$, and c) $\boldsymbol{S3}$.

Table 3 shows the x_l/l values at which the vertical profiles were generated, together with a reference diagram for a better understanding of their location.

Table 3. Location, x_l/l, on steps A and G of $S1$, $S2$, and $S3$.

Steps	x_l/l **of** $S1$	x_l/l **of** $S2$	x_l/l **of** $S3$
Step A	0.20	0.70	0.90
Step G	0.10	0.52	0.73
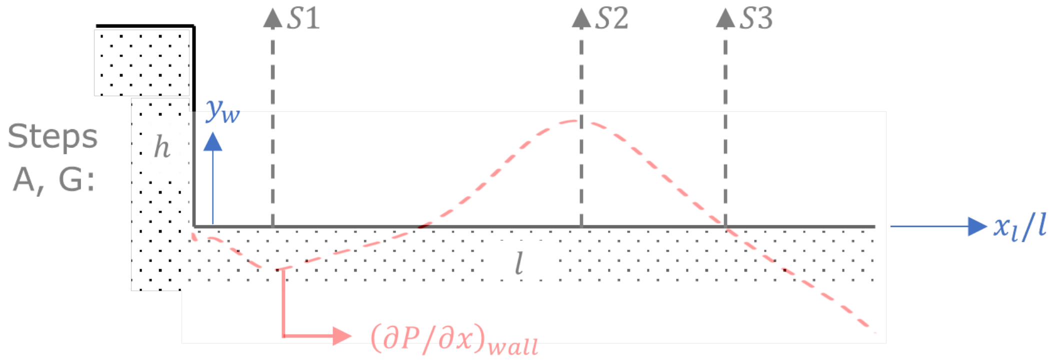			

The velocity magnitude profiles in the separation zone in both the SRV-IZ (Figure 10a) and BRV-IZ (Figure 10b) show two local maxima. The first of lower magnitude, occurs near the tread where the recirculating flow moves parallel to the bottom. Above, the velocity begins to increase at a higher rate at the boundary of the separation zone with the main flow over the pseudo-bottom ("BRV boundary" in Figures 10a and 10b). The distance y_w to this boundary is smaller in $S2$ than in $S1$, as the BRV becomes flatter at closer proximity to the RP. The second maximum of greater magnitude occurs in the main stream and is located closer to the separation zone in the convex curve (step A), while closer to the free surface in the concave curve (step G). This behavior is associated with the location of curves 1 and 2, since in the first one the boundary layer has not intercepted the free surface, so the main stream flow presents an approximately uniform profile. In the second curve the interception has already occurred, so the velocity continues to increase as the distance y_w grows, and finally decreases at the free surface due to friction with the atmospheric air.

At the beginning of the reattachment zone (Figure 10c), only the maximum value of velocity magnitude associated with the stream over the pseudo-bottom is presented, since the one associated with the vortex zone disappears. It is worth noting that the velocity magnitude is higher for the whole height of the flow in the concave curve, for $S1$, $S2$ and $S3$, because it is closer to the final discharge, where the potential energy of the flow at the crest of the channel has transformed into kinetic energy. When comparing with the velocity fields reported by Ashoor and Riazi (2019), multiple coincidences are found. Those authors also showed the local maximum in the separation zone near the tread, and above a minimum in the center of the BRV ("BRV minimum" in Figure 10a of the present study). Furthermore, in their modeling, the local maximum near the free surface also appears in the final section of the stepped channel.

In Figure 10a, two maximum values of the pressure for the steps of both curves were presented, the first at the bottom of the channel in the separation zone, and the second in the main stream at a greater distance y_w for step A than for G. Both maxima are higher in the concave curve.

This shape of the profiles was also reported experimentally and numerically by Saqib *et al.* (2022). On the other hand, negative values of gauge pressure are present in the convex curve, coinciding with the upper corner of the riser, $y_w \sim (h = 0.038m)$. Suction pressures at the step corners have also been reported by Sarkardeh *et al.* (2015). Note that, at this same location the local minimum on the concave curve is far from negative. At $S2$ (Figure 10b), there are no suction pressures, and the local minimum in the separation zone is imperceptible in both steps, completely disappearing in the reattachment zone (Figure 10c). In general, the higher pressures in step G for the whole flow depth are associated with the previously described behavior of streamlines in vertical curves: they tend to move away from the bottom in the convex one, but to compress it in the concave one.

Finally, the three vertical dissipation profiles in the concave curve are higher than in the convex curve, confirming the results of Figure 9b. The geometry of the vertical curve corresponding to step G, added to the fact that it receives the high velocity flow that has fallen down the stepped chute, leads to an increase in shear stresses between the flow and the bottom, and between the fluid layers themselves. This increase in the dissipation rate as the flow advances through the steps, until reaching maximum values at the final absc. of the channel, was also evidenced in the dissipation field reported by Bombardelli *et al.* (2011).

In Figure 10a, in the SRV-IZ, two local maxima of ε are observed in each profile, a smaller one near the bottom due to velocity gradients between the recirculating flow and the wall, and a larger one coinciding with the upper boundary of the BRV, and due to the velocity gradients between the vortex and the stream over the pseudo-bottom. In $S2$, where the recirculating vortex flattens and its boundary approaches the wall, the two maxima of each profile are so close that they appear to merge into one ("two local maxima" in Figure 10b). The maximum of ε along the boundary of the separation zone with the main flow is observed in the results of Bombardelli *et al*. (2011), however, they reported zero dissipation near the bottom. Considering that the authors used wall functions as boundary condition for turbulence, which allow modeling the flow from the logarithmic zone, this may suggest the importance of modeling the closest region of the boundary layer, with the objective of capturing the maximum values of ε due to friction with the tread. Even so, further research in this regard is recommended.

At the beginning of the reattachment zone, the maximum dissipation is achieved only by friction with the solid bottom, showing a single maximum in both steps. Note that both in this zone (Figure 10c) and in the zone of maximum adverse pressure gradient (Figure 10b), the maximum dissipation values for step G are 144 and 138 m^2/s^3, respectively, however, the graphs are interrupted at 45 m^2/s^3 to achieve a better visualization of the maximums of step A. It is worth noting that, for all three profiles at steps A and G, the local maxima of ε near the free surface of the flow are produced by the velocity gradients located at the water-air interface.

The vorticity magnitude ($|\omega_i|$) is calculated considering only the component in the z direction (ω_z), since being a 2D model, $\omega_x = \omega_y = 0$. Equation (14) is then used:

$$|\omega_i| = \sqrt{{\omega_z}^2} = \sqrt{\left(\frac{\partial U_y}{\partial x} - \frac{\partial U_x}{\partial y}\right)^2} \tag{14}$$

Figure 11a presents the $|\omega_i|$ field in the entire stepped channel, to compare its behavior in the separation and reattachment zones of the concave and convex curves and of the straight section. In general, the zones of maximum vorticity coincide with the free surface and the pseudo-bottom. The former corresponds to the velocity gradients between the water flow and the air. The second corresponds to the gradients between the main flow and the recirculation zones in the step cavities. Figure 11b shows a zoom to the field on the convex curve with a detail of step A. In the separation zone of the latter, the maximum vorticity is observed around the streamline at the boundary of the large recirculation vortex (BRVB dashed line) with the main flow, which intercepts the footprint in the RP. This high gradient zone is responsible for the production of turbulence, and for the dissipation maxima shown previously in the corresponding panels of Figures 10a and 10b. In the SRV zone, another region of high vorticity is observed, corresponding to the velocity gradients at the boundary with the counter rotating BRV. Downstream of the RP, the high vorticity zone is given by the gradients generated by the friction of the flow with the tread. The maximum step vorticity is found there, which extends downstream of the right end of the tread, towards the beginning of the subsequent step separation zone. This behavior agrees with the experimental results of Amador, Sánchez-Juny and Dolz (2006), who applied a particle image velocimetry technique to obtain the flow field in a stepped channel with 1V:0.8H slope. The maximum vorticity values reported in that study also occur just downstream of the outer corners of the steps, in a region of low relative thickness. This phenomenon is attributed, according to the authors, to the rapid appearance of small-scale vortices detached from these corners.

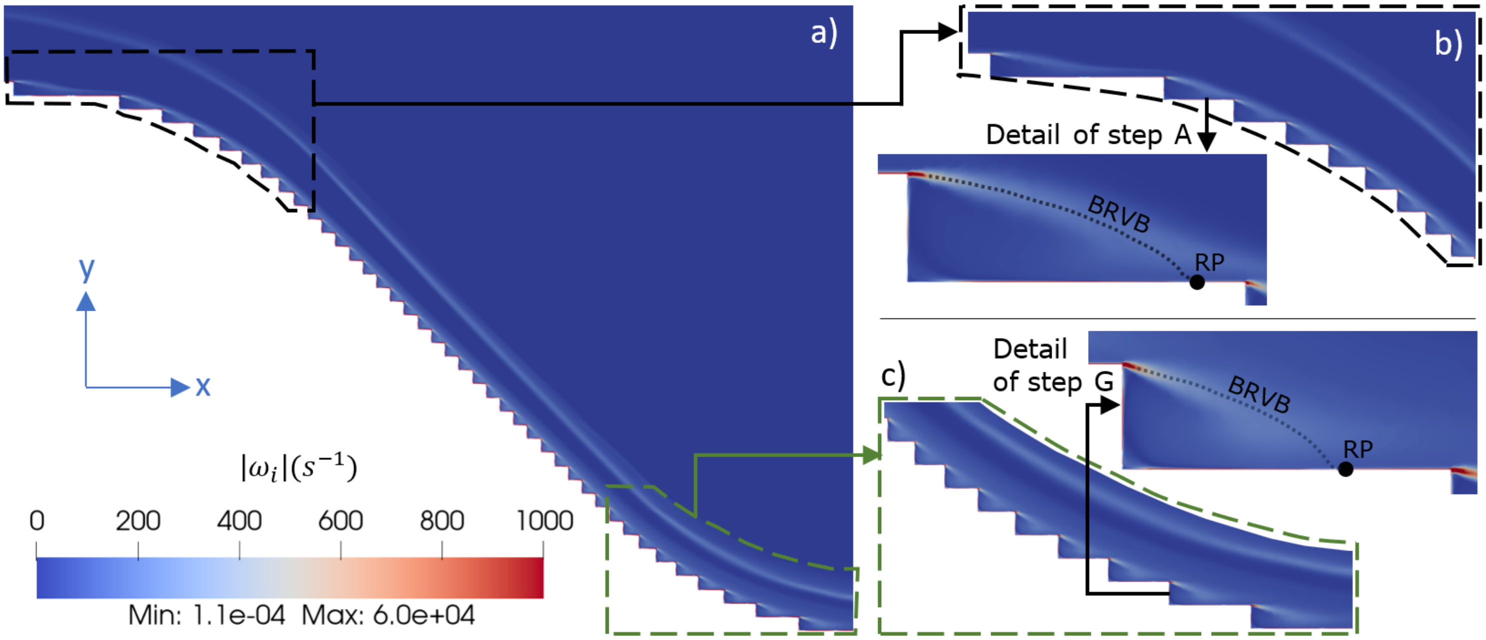

Figure 11. Vorticity magnitude field $|\boldsymbol{\omega}_i|$ in a) the whole channel with vertical curves, b) the convex curve with a detail of step A, c) the concave curve with a detail of step G.

The vorticity field pattern described for the cavities of curve 1 is replicated in those of the straight section and in those of curve 2. The main difference lies in the location of the intersection with the tread, of the high $|\omega_i|$ zone around the BRVB. In the straight chute, the maximum vorticity levels extend between the outer corners of consecutive steps, like the results of Amador *et al.* (2006). This is attributed to the slope, corresponding to an SK3 subregime with the separation zone occupying almost the whole tread. Figure 11c shows a zoom of the concave curve with a detail of step G. The main difference with the convex curve is that the high $|\omega_i|$ zone intercepts in the RP further upstream, which is due to a lower occupancy of the separation zone. Adding to the above, the maximum vorticity of the entire channel at the outer corners occurs at this final curve and is approximately $6.0\mathrm{e}+04s^{-1}$ (note that this maximum is specified under the color bar legend in Figure 11, which is interrupted at $1000s^{-1}$ for better visualization of the field).

Figure 12a presents the k field throughout the stepped channel. In general, the maximum turbulence levels occur near the pseudo-bottom, which confirms the role of the high velocity gradients evidenced in the vorticity field around the BRVB as a zone of high k production. The region occupied by the maximum k values expands towards the free surface in the flow direction, like that evidenced in the results of Amador *et al.* (2006) and Bombardelli *et al.* (2011), who attributed it to the development of the boundary layer. This can be confirmed in Figure 11a, in which the expansion of the zone of maximum velocity gradients is observed in the downstream direction, causing the fraction of the flow depth that contributes to the production of turbulence to increase as the distance from the crest of the channel increases. When comparing the details of the convex and concave curves, in Figures 12b and 12c, respectively, the higher values of k are observed in the second one. Regarding the difference between the separation and reattachment zones, in both curves the highest turbulence is found in the zone of impact of the main stream with the final fraction of the tread.

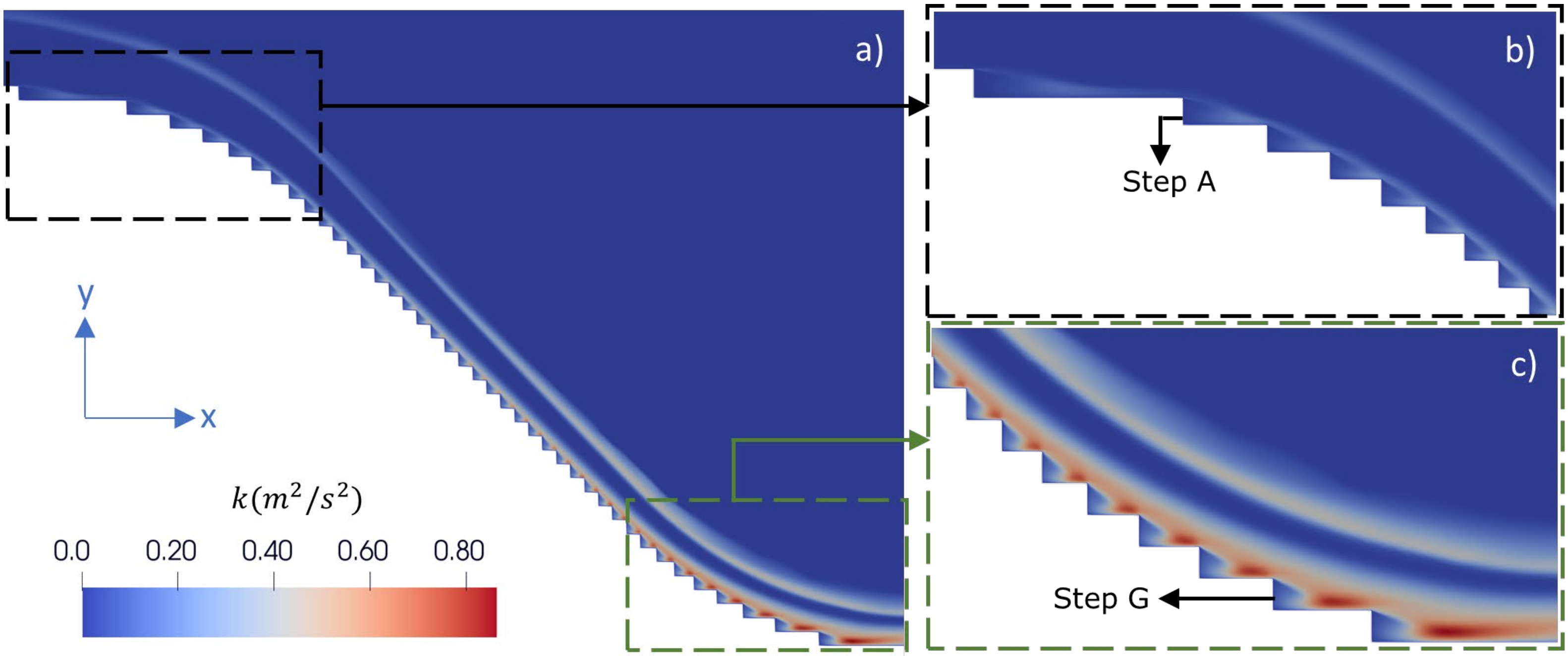

Figure 12. a) Turbulent kinetic energy $\boldsymbol{k}$ field in the whole channel with vertical curves, b) detail of the convex curve, c) detail of the concave curve.

Conclusions

The RNG $k-\varepsilon$ model adequately captures the experimental velocity profiles in the non-aerated flow zone, resulting in a maximum average error per profile of 5 %. Downstream of the air inception point, although the numerical profiles capture the shape of the experimental ones, the average error is larger and the quality of the fit decreases in the flow direction. Near the bottom, in a layer thickness of approximately 26 % of h, velocity measurements are underestimated, while further away they are overestimated. The increased error in this region is associated with the numerical model not capturing the aeration phenomenon. It is found in the literature that the best option for modeling air entrapment by turbulent disturbance of the free surface is to apply the LES turbulence model. Further research using this simulation technique is recommended, for example, in a stepped concave curve, which is more likely to coincide with the aerated flow because it is located at the discharge of the channel.

The objectives proposed for this study were to establish the fraction of the steps occupied by the vortex and the reattachment flow regions, defining the difference in the distribution of velocity, pressure, vorticity, and turbulence statistics in these zones. The above, to compare the hydrodynamics of the flow in the three sections of the channel: convex curve, straight chute, and concave curve. The conclusions derived from the results of this work, fulfilling the described objectives, are listed below:

1. By means of the numerical modeling of this study in the channel with vertical curves, two main zones were captured in each step, the

separation zone and the reattachment one. In the first one, two recirculation vortices are observed, a large one rotating clockwise, and a small one in the inner corner of the steps, rotating counterclockwise. In the reattachment zone, the main flow impacts the final fraction of the tread and flows to the next step. In the concave curve, the velocities obtained in the separation zone are lower, corresponding to less than 20 % of the maximum velocity in the channel, and in the reattachment zone they are larger, increasing up to 40 %.

2. The small vortex occupies a smaller fraction of the tread in the concave curve than in the convex one, and while in the former the fraction of occupancy decreases step by step in the flow direction, in the latter it increases. On the other hand, the reattachment point is closer to the riser in the concave, so the reattachment zone occupies a larger fraction of the step. This is because at the outlet of the channel, the dynamic forces produced at the bottom by the reduction of the slope compress the separation zone. The opposite effect occurs in the curve at the entrance of the channel, where the streamlines tend to move away from the bottom.

3. In the separation zone near the riser of the steps of the concave and convex curves, two local pressure maxima are found, one near the bottom in the recirculation zone, and the other in the main stream above the pseudo-bottom. In the middle there is a local minimum, negative only in the convex curve and located approximately at the top corner of the riser. In the separation zone near the reattachment point, and in the reattachment zone this local minimum disappears in both step curves, resulting in a maximum pressure at the bottom of

the channel, which decreases as a function of the distance from the wall. The analyzed profiles showed in general that, at the whole flow depth, the pressure is higher in the concave curve than in the convex one.

4. Regarding turbulent kinetic energy dissipation, it is evident that the small vortex does not generate a significant contribution to this variable at any step of the channel. Near the bottom, dissipation occurs mainly in the big recirculation vortex and in the reattachment zone. In the latter, it is greater along the entire channel and is produced by the friction of the flow with the last section of each step. Similar to what was concluded for the pressure, in the direction perpendicular to the tread of both vertical curves, two local dissipation maxima are found in the separation zone. A maximum near the bottom due to velocity gradients between the recirculating flow and the wall, and a larger maximum coinciding with the upper boundary of the separation zone, and due to the velocity gradients between the vortex and the flow over the pseudo-bottom. These two maxima approach each other until they merge into one as the large vortex flattens near the reattachment point. Finally, the analyzed profiles showed in general that, for the whole flow depth, turbulent dissipation is greater in the concave curve than in the convex one.
5. The maximum vorticity in the step separation zone occurs around the boundaries between the main stream and the big vortex, and between the latter and the small vortex. In the reattached flow zone the magnitude is larger and is given by the velocity gradients generated by the tread. There, the zone of maxima extends downstream towards

the beginning of the subsequent step separation zone. The vorticity magnitude increases in the flow direction, with the maximum values being found near the outer corners of the steps of the concave curve.

6. Zones of high vorticity associated with high gradients in the flow, correlated with regions of turbulent kinetic energy production. The maximum levels of k were then found around the pseudo-bottom for the separation zone, and above the tread for the reattachment zone, being larger in the latter. Both the magnitude of k and the fraction of the depth encompassed by high levels of turbulence increased in the flow direction, finding their maximum values in the concave curve at the channel outlet.

References

Amador, A., Sánchez-Juny, M., & Dolz, J. (2006). Characterization of the nonaerated flow region in a stepped spillway by PIV. *Journal of Fluids Engineering*, *128*(6), 1266. DOI: 10.1115/1.2354529

Ansys Inc. (2022). *ANSYS Fluent User's Guide* (Vol. 2022 R2).

Arjenaki, M. O., & Sanayei, H. R. Z. (2020). Numerical investigation of energy dissipation rate in stepped spillways with lateral slopes using experimental model development approach. *Modeling Earth Systems and Environment*, 6(2), 605-616. DOI: 10.1007/S40808-020-00714-Z/METRICS

Ashoor, A., & Riazi, A. (2019). Stepped spillways and energy dissipation: A non-uniform step length approach. *Applied Sciences*, 9(23), 5071. DOI: 10.3390/app9235071

Attari, J., & Sarfaraz, M. (2012). Transitional steps zone in steeply sloping stepped spillways. *9th International Congress on Civil Engineering*, *9*. Recuperado de https://civilica.com/doc/165678/certificate/print/

Boes, R. M., & Hager, W. H. (2003). Two-phase flow characteristics of stepped spillways. *Journal of Hydraulic Engineering*, 129(9), 661-670. DOI: 10.1061/(ASCE)0733-9429(2003)129:9(661)

Bombardelli, F. A., Meireles, I., & Matos, J. (2011). Laboratory measurements and multi-block numerical simulations of the mean flow and turbulence in the non-aerated skimming flow region of steep stepped spillways. *Environmental Fluid Mechanics*, 11(3), 263-288. DOI: 10.1007/S10652-010-9188-6/METRICS

Bureau of Reclamation. (1987). *Design of small dams* (3rd ed.). Washington, DC: US Government Printing Office. Recuperado de https://www.usbr.gov/tsc/techreferences/mands/mands-pdfs/SmallDams.pdf

Casa, E., Hidalgo, X., Castro, M., Ortega, P., & Vera, P. (2018). Modelación numérica del flujo rasante en una rápida escalonada aplicando la dinámica de fluidos computacional (CFD) mediante el uso de Flow-3D. *Revista Politécnica*, 41(2), 53-64. Recuperado de https://revistapolitecnica.epn.edu.ec/ojs2/index.php/revista_politecnica2/article/view/823

Chahed, J., Roig, V., & Masbernat, L. (2003). Eulerian-Eulerian two-fluid model for turbulent gas–liquid bubbly flows. *International Journal of Multiphase Flow*, 29(1), 23-49. DOI: 10.1016/S0301-9322(02)00123-4

Chanson, H. (1994). Hydraulics of skimming flows over stepped channels and spillways. *Journal of Hydraulic Research*, 32(3), 445-460. DOI: 10.1080/00221689409498745

Chanson, H. (2001). Hydraulic design of stepped spillways and downstream energy dissipators. *Dam Engineering*, 11(4), 205-242.

Chanson, H., & Toombes, L. (2004). Hydraulics of stepped chutes: The transition flow. *Journal of Hydraulic Research*, 42(1), 43-54.

Cheng, X., Luo, L., Zhao, W., & Li, R. (2004). Two-phase flow simulation of aeration on stepped spillway. *Progress in Natural Science*, 14(7), 626-630. DOI: 10.1080/10020070412331344051

Chinnarasri, C., & Wongwises, S. (2006). Flow patterns and energy dissipation over various stepped chutes. *Journal of Irrigation and Drainage Engineering*, 132(1), 70-76. DOI: 10.1061/(ASCE)0733-9437(2006)132:1(70)

Cifani, P., Michalek, W. R., Priems, G. J. M., Kuerten, J. G. M., van der Geld, C. W. M., & Geurts, B. J. (2016). A comparison between the surface compression method and an interface reconstruction method for the VOF approach. *Computers & Fluids*, 136, 421-435. DOI: 10.1016/J.COMPFLUID.2016.06.026

Dalili-Khanghah, K., & Kavianpour, M. R. (2020). Numerical investigation of the effect of CEDEX profile on the hydraulic parameters in the stepped spillway and the performance of this profile in various chute slopes. *Iranian Journal of Science and Technology - Transactions of Civil Engineering*, 44(4), 1247-1254. DOI: 10.1007/S40996-019-00313-8/FIGURES/8

Escue, A., & Cui, J. (2010). Comparison of turbulence models in simulating swirling pipe flows. *Applied Mathematical Modelling*, 34(10), 2840-2849. DOI: 10.1016/J.APM.2009.12.018

Gonzalez, C. A. (2005). *An experimental study of free-surface aeration on embankment stepped chutes*. Recuperado de https://espace.library.uq.edu.au/view/UQ:158019

Greenshields, C. (2022). *OpenFOAM v10 User Guide*. London, UK: The OpenFOAM Foundation. Recuperado de https://doc.cfd.direct/openfoam/user-guide-v10

Greenshields, C., & Weller, H. (2022). *Notes on computational fluid dynamics: General principles*. Reading, UK: CFD Direct Ltd. Recuperado de https://doc.cfd.direct/notes/cfd-general-principles/index/

Henrique-Povh, P., & Junji-Ota, J. (2019). Transition stretch of spillways with bevelled steps. *38th IAHR World Congress - 'Water: Connecting the World'*, 38, 1520-1528. DOI: 10.3850/38WC092019-1065

Hirt, C. W. (2003). Modeling turbulent entrainment of air at a free surface. *Technical Note 61*(FSi-03-TN61). Pasadena, USA: Flow Science Inc.

Hirt, C. W., & Nichols, B. D. (1981). Volume of fluid (VOF) method for the dynamics of free boundaries. *Journal of Computational Physics*, 39(1), 201-225. DOI: 10.1016/0021-9991(81)90145-5

Hunt, S., & Kadavy, K. (2010a). Energy dissipation on flat sloped stepped spillways: Part 1. Upstream of the inception point. *Transactions of the American Society of Agricultural and Biological Engineers*, 53(1), 103-109.

Hunt, S., & Kadavy, K. (2010b). Energy dissipation on flat sloped stepped spillways: Part 2. Downstream of the inception point. *Transactions of the American Society of Agricultural and Biological Engineers*, 53(1), 111-118.

Kundu, P. K., Cohen, I. M., & Dowling, D. R. (2012). *Fluid Mechanics* (5th ed.). Oxford, UK: Elsevier Inc. DOI: 10.1016/C2009-0-63410-3

Llano, S. (2003). *Hydraulics of Stepped structures - importance of flow regimes on stepped chutes and practical application in developing countries*. Delft, Netherlands: IHE Delft Institute for Water Education.

Matos, J., Frizell, K. H., André, S., & Frizell, K. W. (2002). On the performance of velocity measurement techniques in air-water flows. In: *Hydraulic measurements and experimental methods 2002* (pp. 1-11). Reston, USA: American Society of Civil Engineers. DOI: 10.1061/40655(2002)58

Medhi, B. J., Singh, A., Thokchom, A. K., & Mahapatra, S. (2019). Experimental and computational study on flow over stepped spillway. *Journal of Mechanical Science and Technology*, 33(5), 2101-2112. DOI: 10.1007/S12206-019-0116-5/METRICS

Nikseresht, A. H., Talebbeydokhti, N., & Rezaei, M. J. (2013). Numerical simulation of two-phase flow on step-pool spillways. *Scientia Iranica*, *20*(2), 222–230. DOI: 10.1016/j.scient.2012.11.013

Orszag, S. A., Yakhot, V., Flannery, W. S., & Boysan, F. (1993). Renormalization group modeling and turbulence simulations. On *near-wall turbulent flows*. *Near-wall turbulent flows: Proceedings of the International Conference on Near-Wall Turbulent Flows*, Tempe, Arizona, USA, 15-17 March 1993, Elsevier Publishing Company.

Saqib, N. U., Akbar, M., Pan, H., Ou, G., Mohsin, M., Ali, A., & Amin, A. (2022). Numerical analysis of pressure profiles and energy dissipation across stepped spillways having curved risers. *Applied Sciences 2022*, 12(1), 448. DOI: 10.3390/APP12010448

Sarkardeh, H., Marosi, M., & Roshan, R. (2015). Stepped spillway optimization through numerical and physical modeling. *International Journal of Energy and Environment*, 6(6), 597-606. Recuperado de https://www.ijee.ieefoundation.org/

Sotelo-Ávila, G. (2002). *Hidráulica de Canales*. México, DF, México: Facultad de Ingeniería, Universidad Nacional Autónoma de México.

Tabbara, M., Chatila, J., & Awwad, R. (2005). Computational simulation of flow over stepped spillways. *Computers & Structures*, 83(27), 2215-2224. DOI: 10.1016/j.compstruc.2005.04.005

Versteeg, H. K., & Malalasekera, W. (2007). *An introduction to computational fluid dynamics: The finite volume method*. Harlow, England: Pearson Education Ltd.

Wang, F. F., Wu, S. Q., & Zhu, S. L. (2019). Numerical simulation of flow separation over a backward-facing step with high Reynolds number. *Water Science and Engineering*, 12(2), 145-154. DOI: 10.1016/J.WSE.2019.05.003

Wilcox, D. C. (2006). *Turbulence modeling for CFD* (3rd ed.). La Cañada, California: DCW Industries, Inc.

Yakhot, V., Orszag, S. A., Thangam, S., Gatski, T. B., & Speziale, C. G. (1992). Development of turbulence models for shear flows by a double expansion technique. *Physics of Fluids A*, 4(7), 1510-1520. DOI: 10.1063/1.858424

Zare, H. K., & Doering, J. C. (2012). Effect of rounding edges of stepped spillways on the flow characteristics. *Canadian Journal of Civil Engineering*, 39(2), 140-153. DOI: 10.1139/L11-121

Zhan, J., Zhang, J., & Gong, Y. (2016). Numerical investigation of air-entrainment in skimming flow over stepped spillways. *Theoretical and Applied Mechanics Letters*, 6(3), 139-142. DOI: 10.1016/J.TAML.2016.03.003

Zuhaira, A. A., Al-Hamd, R. K. S., Alzabeebee, S., & Cunningham, L. S. (2021). Numerical investigation of skimming flow characteristics over non-uniform gabion-stepped spillways. *Innovative Infrastructure Solutions*, 6(4). DOI: 10.1007/S41062-021-00579-W